

Impact of Angle-Voltage Coupling on Small-Signal Stability of Power Systems: A Damping Perspective

Xiaoyu Peng, Cong Fu, Peng Yang, Xi Ru, Feng Liu, *Senior Member, IEEE*

Abstract—The rise of inverters integrated into power systems has raised enormous concerns about potential system instability. This paper aims to investigate the correlation between phase-angle and voltage dynamics and their impacts on the stability of power systems, focusing on damping perspectives. To this end, we first formulate a generic model to unify the dynamics of synchronous generators and diverse inverter-interfaced devices. By exploring systems' damping characteristics, we find that angle-voltage coupling tends to undermine stability by redistributing the system's damping in a more dispersed manner, consequently rendering the system more vulnerable to inadequate or even negative damping. Our work also involves analyzing and quantifying the factors affecting coupling strength, including power flow, control parameters of devices, and the number of integrated inverters. A cross-loop control is also introduced to demonstrate the potential benefits of utilizing angle-voltage coupling to enhance stability. We validate these findings through simulations on a modified IEEE 39-bus system with heterogeneous inverters and other standard benchmarks with up to 500 buses. Simulations show the coupling's impact on dispersing individual damping under 100% of the tested benchmarks. The rightmost eigenvalue shift varies from 20% to 80% under the coupling, which significantly influences the stability evaluation results. This comprehensive investigation yields insights into the complexities of angle-voltage coupling, which offers useful implications for the analysis and control of power systems.

Index Terms—Inverter-dominant power systems, power system dynamics, power system stability, angle-voltage coupling, damping, eigenvalue distribution.

I. INTRODUCTION

A. Background and Motivation

THE increasing penetration of renewable resources with inverter interfaces has brought about remarkable changes in stability characteristics of power systems in recent years [1]. Traditional power systems, primarily reliant on synchronous generators (SGs), often encounter rotor-angle or voltage stability issues under specific conditions. Unlikely, current systems with integration of numerous inverter-interfaced devices present much more complex stability challenges, partially due to the strong coupling between phase-angle and voltage dynamics, referred to as *angle-voltage coupling*.

Received 11 February; revised 21 August, accepted 06 October. This paper is supported by the Science and Technology Project of China Southern Power Grid Co., Ltd under Grant 036000KC23090004 (GDKJXM20231026). (Corresponding Author: Feng Liu).

Xiaoyu Peng, Xi Ru, and Feng Liu are with the Department of Electrical Engineering, Tsinghua University, Beijing, China (email: pengxy19@tsinghua.org.cn; thu.ruxi@gmail.com; lfeng@tsinghua.edu.cn).

Cong Fu is with Guangdong Power Grid Co., Ltd, Guangzhou, China (email: 609511305@qq.com).

Peng Yang is with the School of Electronics and Information, Xi'an Polytechnic University, Xi'an, China (email: p-yang13@tsinghua.org.cn).

In traditional power systems dominated by SGs, phase-angle and voltage dynamics are usually analyzed independently due to their differing timescales [2]. However, in inverter-dominant power systems, both dynamics are simultaneously generated on overlap timescales, leading to strong coupling in stability issues [1]. Theoretical research has highlighted the impact of voltage dynamics on synchronization [3]–[5] and frequency dynamics [6], while practices have observed instances of coupled oscillatory instability and loss of synchronization due to voltage problems [7]–[9]. Therefore, angle-voltage coupling turns out to be crucially important to the stability of future inverter-dominant power systems. Nonetheless, notwithstanding its growing significance, research on angle-voltage coupled stability remains in its nascent stages, with its underlying mechanisms still presenting unresolved challenges, thereby primarily motivating our investigations.

B. Literature Review

As previously discussed, in systems with relatively independent phase-angle and voltage dynamics, the dominant factor driving instability is often singular [1]. Therefore, previous research focused on identifying the leading factor of transient phase-angle and voltage instability using data-driven methods [10] and transient energy flow methods [11]. However, when the system lacks a single dominant instability mode—meaning phase-angle and voltage subsystems contribute equally to instability—such identification loses theoretical justification.

Detailed analysis of how angle-voltage coupling impacts power system stability remains an emerging field. Existing limited research primarily follows two approaches: eigenvalue-estimation-based methods and energy-function-based methods.

(1) *Eigenvalue-estimation-based methods*: These methods analyze the impact of coupling by estimating the direction and magnitude of rightmost eigenvalue (critical eigenvalue) shifts under coupling effects. In the literature, [12] pioneered order-reduced stability analysis considering angle-voltage coupling. [13] further demonstrated that in pure SG-integrated systems, phase-angle dynamics invariably participate in voltage small-disturbance instability. Building on this, the method was extended to power systems with lossy transmission lines using matrix perturbation techniques [14]. Additionally, [15] reveals that the network coupling reversal could induce system desynchronization. Estimating critical eigenvalues poses significant challenges, especially in high-dimensional systems [16]. Consequently, to obtain rigorous analytical results, these methods rely on strong model assumptions. Specifically, they confine device models to third-order SG-resembling structures, leveraging their symmetry for analytical simplification. However,

the behavior of widely integrated inverter dynamics—such as P - f and Q - V droop strategies—lacks such symmetry, limiting these methods' applicability to angle-voltage coupling analysis in inverter-dominant systems.

(2) *Energy-function-based methods*: They have a long history in power system stability studies and can extend to large-disturbance stability analysis. Classical approaches typically assume constant voltage to ignore angle-voltage coupling for constructing rigorous energy functions [17]. To address this limitation, [18] integrates the inverter Q - V control loop as algebraic equations into the active power control loop. However, this treatment neglects voltage dynamics. Alternatively, [19] analyzes angle-voltage coupling from a passivity perspective, arguing that coupling creates new instability pathways and transient energy supply routes, subsequently deriving distributed sufficient conditions for stability under coupling. Still, a well-known limitation persists for energy-function-based methods: during energy function construction, frequency damping is often incorporated as a term ensuring negative definiteness of the derivative of energy functions (e.g., $\dot{V} \leq -d\omega^2 + \text{other negative terms}$). Therefore, they are excluded from the energy function's explicit form and not reflected in the corresponding indices. Even with various extensions, its application in inverter-integrated systems remains restricted [20], [21]. Crucially, damping significantly suppresses coupling and enhances stability. The lack of quantifying the damping's impact on coupling strength substantially compromises the accuracy of these methodologies.

Beyond these two approaches, emerging developments exist. An important contribution to the field is the theory of complex frequency, which aims to extend the phasor model to angle-voltage analysis. Despite progress in coupled control [22], [23], quantifying coupling's impact on stability in heterogeneous device environments remains challenging [24]. Meanwhile, transfer function-based coupling analysis—widely adopted in power electronics—can directly incorporate electromagnetic transients [3]. However, these methods predominantly focus on single-inverter systems, making them challenging to extend to multi-machine meshed systems where device interactions critically influence stability.

Inverter control is another concern when considering the angle-voltage coupling. Previous studies focus on decoupling methods especially for high R/X grids, such as virtual impedance or power compensation [3], [25]. However, even pure inductive grids might have significant coupling issues, as indicated by this paper. Besides, simply minimizing the impact of coupling may not be the most effective approach to enhancing the stability of interconnected systems, given the capacity limitations of inverters. An innovative approach involves leveraging the coupling to improve system stability through *cross-loop controls* that integrate voltage and frequency feedback into control loops [22], [23], [26], [27]. While sharing fundamental concepts, their diversity in control configurations and parameter adjustment largely prevents them from comprehending the mechanism of the coupling impacts.

C. Main Contribution

Key idea: To address these research gaps, this work probes the impact of angle-voltage coupling on stability through the lens of system damping and its distribution. Mathematically, we extend eigenvalue-estimation-based methods by analyzing how coupling terms in the state matrix influence system eigenvalues. However, unlike existing approaches that narrowly estimate shifts in the rightmost eigenvalue, we quantify the collective redistribution of all eigenvalues induced by coupling. Specifically, we prove that coupling disperses eigenvalues away from symmetry, forcing the rightmost eigenvalue toward the imaginary axis and thereby undermining stability (analogous to a *barrel effect*). By focusing on the overall distribution of eigenvalues, the device types that the mechanism can be compatible with have significantly increased. Moreover, by introducing the invariant total damping, we explicitly account for the role of frequency damping—which prior energy-based methods artificially excluded—in counteracting coupling-induced instability. This dual focus overcomes the limitations of model-specific eigenvalue methods and damping-agnostic energy approaches.

Main contribution: By introducing two innovative concepts, *total damping* and *average damping*, we streamline the analysis with a clear interpretation. For the first time, we find that angle-voltage coupling generally undermines system stability by redistributing the damping across the whole system in a more divergent manner instead of reducing the total or average damping, the redistribution strength of which can be quantified by the *damping redistribution index*. In addition, we conduct an analysis of the key factors influencing the strength of coupling, encompassing power flow, dynamic parameters of devices, control strategies, and the number of integrated inverters. The suggested approach provides a fresh perspective on comprehending the stability of inverter-dominant power systems, offering valuable insights for better identification and control design of angle-voltage coupled systems.

D. Organization

The organization of the rest of the paper is shown in Fig. 1. Section II introduces the unified dynamic model and formulates the problem. Section III introduces a damping perspective to understand angle-voltage coupled stability and discover the foundational invariance of total damping. Under these concepts, Section IV demonstrates the novel damping redistribution mechanism underlying the coupling to influence stability. The effect of various factors, including device and system configurations, on the damping redistribution, is analyzed in Section V. The concept and prototype of the cross-loop control are also demonstrated in this section. Then, all results are verified on a heterogeneous IEEE 39-bus system in Section VI. Finally, Section VII concludes the paper.

E. Notation and Symbol

Notation: The real and imaginary parts of a complex number are denoted by $\mathcal{R}(\cdot)$ and $\mathcal{I}(\cdot)$, respectively. $\|\cdot\|$ and $\|\cdot\|_\infty$ denote the matrix norm induced by vector 2-norm and ∞ -norm. For a square matrix, $\det(\cdot)$, $\text{Tr}(\cdot)$ and $\dim(\cdot)$ denote its

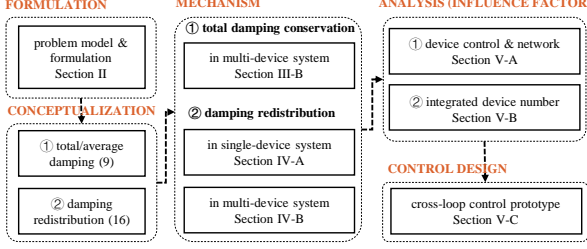


Fig. 1. Framework of this paper.

determinant, trace and dimension respectively. $\lambda(\cdot)$ represents its eigenvalue(s) with the corresponding spectrum denoted as $\{\lambda_i\}$. For a real symmetrical matrix, $\succ 0$ denotes its positive definiteness. The identity matrix, all-zero, and all-one vector/matrix are respectively represented by I , \mathbb{O} , and $\mathbb{1}$.

Symbol: The electrical quantities V , θ , P and Q represent voltage magnitude, phase-angle, active and reactive power, respectively. The state matrix of a linearized power system model is T . Besides, the symbols T_n and T_c denote its non-coupled and cross-coupling terms.

II. MODELING AND PROBLEM FORMULATION

A. Power System Modeling

Consider a n -bus power system abstracted as an undirected graph $\mathcal{G} = G(\mathcal{V}, \mathcal{E})$, where \mathcal{V} and \mathcal{E} are the set of buses and transmission lines, respectively. For the graph \mathcal{G} , \mathcal{A} denotes its node-branch unweighted incident matrix. The angle-voltage coupling exists on a wide bandwidth with distinct mechanisms. In this paper, we focus on the electromechanical transient processes, and thus, the phasor model is employed. Then, each bus $i \in \mathcal{V}$ can be represented from its port by $(V_i, \theta_i, P_i, Q_i)$, where the four entries represent voltage magnitude, phase-angle, active, and reactive power injection in order.

Power flow model. As the transmission grids usually have a low R/X ratio, it is common to assume a lossless network. Then the power flow [28] could be expressed as

$$P_i = \sum_{j \in \mathcal{V}} V_i V_j B_{ij} \sin \theta_{ij}, \quad Q_i = - \sum_{j \in \mathcal{V}} V_i V_j B_{ij} \cos \theta_{ij} \quad (1)$$

where susceptance matrix B satisfies $B_{ij} = B_{ji} \geq 0$ and $B_{ii} = - \sum_{j \neq i} B_{ij} < 0$. The possible shunt capacitors can be modeled within device dynamics [29].

Device dynamic model. Each device $i \in \mathcal{V}$ is assumed to satisfy the following generic dynamic model.

$$\begin{aligned} \dot{\theta}_i &= \omega_i \\ M_i \dot{\omega}_i &= -d_i \omega_i - P_i + P_{mi} \\ \tau_i \dot{V}_i &= -V_i + u_i - r_i \frac{Q_i}{V_i} - g_i Q_i \end{aligned} \quad (2)$$

where ω_i represents the frequency deviation. The dynamic parameters $M_i, d_i, \tau_i, r_i, g_i \geq 0$ usually hold for well-designed devices. The proposed model provides a uniform representation for some acknowledged phase-angle/frequency and voltage dynamics as shown below:

- The phase-angle and frequency dynamic can represent various devices such as SGs, and inverters with virtual-SG or virtual-inertia control.
- As for the voltage dynamics, it is demonstrated in [29] that SGs and inverters with reactive current control can be transformed in this form with $g_i = 0$. Additionally, the inverters with $Q - V$ droop control as shown in (3) could be represented by setting $r_i = 0$, $\tau_i = \tau_{dpQ,i}$, $u_i = V_{set,i} + D_{dpQ,i} Q_{set,i}$ and $g_i = D_{dpQ,i}$.

$$\tau_{dpQ,i} \dot{V}_i = -(V_i - V_{set,i}) - D_{dpQ,i} (Q_i - Q_{set,i}) \quad (3)$$

In brief, the model (2) can represent various inverter-interfaced devices, as summarized in Fig. 2. Due to its generality, the following analysis will be based on this model.

Remark 1. The proposed model also applies to the first-order phase-angle dynamics (4) to model $P - \theta$ droop-controlled inverters, as discussed in Section IV-D.

$$\zeta_i \dot{\theta}_i = -\eta_i (\theta_i - \theta_{set,i}) - (P_i - P_{set,i}) \quad (4)$$

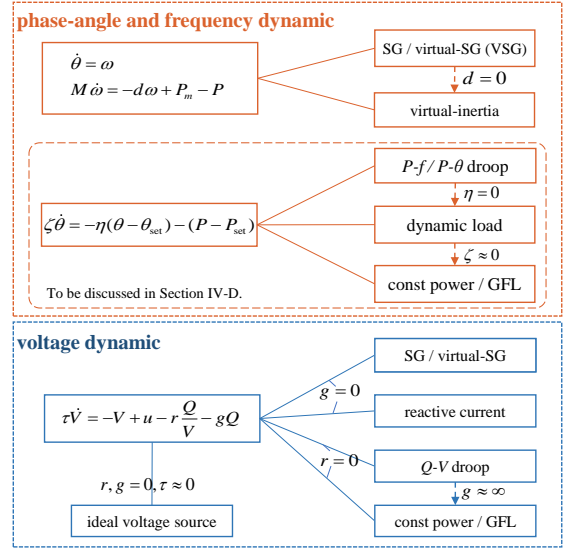


Fig. 2. Applicable devices for proposed generic dynamic model.

Remark 2. The grid-following (GFL) inverters are modeled as constant power sources, which reflects the power source characteristics in electromechanical transient as demonstrated in [30]. In this sense, GFL devices can be viewed as the GFM devices with zero active stability support capability, thus enabling a comparable analysis between both GFM and GFL devices. The analysis considering detailed GFL models with phase-lock loops (PLLs) is still under investigation. Despite those GFL devices, all dynamics in Fig. 2 are grid-forming (GFM) devices.

Without loss of generality, we assume the equilibrium $[\theta^{*T}, \omega^{*T}, V^{*T}]^T$ exists. This assumption excludes the instability caused by the vanishment of equilibrium, such as saddle-node or limit-induced bifurcation.

Assumption 1. An isolated equilibrium exists for system \mathcal{G} .

As we focus on the coupling dynamics under small-signal disturbance, the system \mathcal{G} can be locally linearized around the equilibrium with Assumption 1 satisfied, which yields the linear system \mathcal{LG}

$$\mathcal{LG} : \frac{d}{dt} [\Delta\theta^T, \Delta\omega^T, \Delta V^T]^T = T [\Delta\theta^T, \Delta\omega^T, \Delta V^T]^T \quad (5)$$

where Δ represents the incremental value compared with its steady value. The state matrix T is defined as

$$\begin{aligned} & \left[\begin{array}{ccc} \mathbb{O} & I & \mathbb{O} \\ -M^{-1}A & -M^{-1}d & -M^{-1}D \\ -\bar{\tau}^{-1}(\bar{r}\bar{D}^T + \bar{g}\bar{E}) & \mathbb{O} & -\bar{\tau}^{-1}(\bar{r}\bar{C}_1 + \bar{g}\bar{C}_2 + \bar{I}) \end{array} \right] \\ & = \begin{bmatrix} T_\theta & T_{\theta V} \\ T_{V\theta} & T_V \end{bmatrix} \end{aligned} \quad (6)$$

where $M = \text{diag}(M_1, M_2, \dots, M_n)$ and similar to d , τ , r and g . The entry-wise expression of the coefficient matrices A , C_1 , C_2 , D and E are given in Appendix A of [31].¹

B. Problem Formulation

The state matrix T can be split into two parts, the non-coupling part T_n and the coupling part T_c .

$$T = \begin{bmatrix} T_\theta & T_{\theta V} \\ T_{V\theta} & T_V \end{bmatrix} = \begin{bmatrix} T_\theta & \\ & T_V \end{bmatrix} + \begin{bmatrix} & T_{\theta V} \\ T_{V\theta} & \end{bmatrix} \stackrel{\text{def}}{=} T_n + T_c \quad (7)$$

Traditional phase-angle and voltage dynamics are usually treated separately in stability analysis, which implies only T_n is considered while their coupling T_c is omitted. It is reasonable for SG-dominant power systems as typically we have $\|T_c\|_F/\|T\|_F \approx 10^{-2} \approx 0$ in practice, where $\|\cdot\|_F$ is the Frobenius norm. However, inverter-dominant systems are not the case due to the inescapable phase-angle and voltage dynamic interaction, where $\|T_c\|$ is significant to stability evaluation results. In this context, a few questions arise naturally:

- Does the coupling lead to a negative influence on the stability?
- If so, how does the negative influence perform, and what factor is it related to?
- Is there any approach to reduce the negative influence and enhance the stability?
- Despite its inaccuracy, when are the results of decoupled analysis acceptable?

These questions will be discussed in order in the next sections.

Remark 3 (Physical Origination of Angle-Voltage Coupling). The angle-voltage coupling in this paper originates from the network impedance, considering the device control strategies (2) are decoupled. The network-induced coupling is widely acknowledged, see [3], [15], [32], [33] for example. Clearly, if the network power flow equations are not coupled, i.e., $D = \partial P / \partial V = (\partial(Q/V) / \partial\theta)^T = 0$ and $E = \partial Q / \partial\theta = 0$, we obtain $T_{\theta V} = T_{V\theta} = 0$ in (6) and thus the state matrix T would be non-coupled. On the other hand, the

¹Because of the space limitation, all appendices in this article are omitted. The full version, including all appendices, can be found in [31].

coupling strength is also influenced by the inverter dynamics. Mathematically, the anti-diagonal terms $T_{\theta V}$ and $T_{V\theta}$ are also influenced by the device dynamic control strength parameters r , g and the device dynamic time-constant parameters M , τ .

C. Well-posedness of Angle-voltage Coupled Stability Problem

This part regulates the well-posedness of the coupled stability problem. Firstly, the domain of definition is restricted. Since the subspace $\Delta\theta = \text{span}(\mathbb{1})$ corresponds to the rotation symmetry of power flow, it can be excluded without physically influencing the stability. In computation, it is implemented by introducing a reference bus for θ .

Definition 1. The definition domain of state variables is $\mathcal{D}_f = \{[\Delta\theta^T, \Delta\omega^T, \Delta V^T]^T : \Delta\theta \perp \mathbb{1}\}$.

Generally, it is unnecessary to consider the coupled stability when the phase-angle or voltage subsystem loses stability individually. Therefore, we assume T_θ and T_V are Hurwitz as we are only interested in the coupled stability of T .

Lemma 1. Suppose Assumption Each $(i, j) \in \mathcal{E}$ satisfies $|\theta_{ij}^*| \in (0, \pi/2)$. Besides, T_V is Hurwitz on \mathcal{D}_f . Then, the non-coupled state matrix T_n is Hurwitz on \mathcal{D}_f .

Proof. The proof can be found in Appendix B of [31]. \square

III. DAMPING-BASED PERSPECTIVE TO ANALYZE ANGLE-VOLTAGE COUPLING

A. Universal Existence of Influence

This part confirms that angle-voltage coupling does negatively affect system stability, as indicated by Lemma 2.

Lemma 2. If $T_c \neq \mathbb{O}$, then its largest real part of eigenvalues is positive, i.e., $\max \mathcal{R}(\lambda(T_c)) > 0$.

Proof. Since all diagonal entries of T_c are zeros, we have $\text{Tr}(T_c) = 0 = \sum_i \lambda_i^{(c)}$, where $\{\lambda_i^{(c)}\}$ is the spectrum of T_c . Noticing that $T_c \neq \mathbb{O}$, we conclude $\max \mathcal{R}(\lambda_i^{(c)}) > 0$. \square

Without loss of generality, we consider the diagonalization $T_c = P_c^{-1} \Lambda_c P_c$ and $T_n = P_n^{-1} \Lambda_n P_n$. Suppose the spectrum Λ_c is sorted in descending order of the real parts as $\lambda_1^{(c)}, \lambda_2^{(c)}, \dots, \lambda_{\dim(T)}^{(c)}$, then the linearized system \mathcal{LG} (5) can be equivalently represented as

$$\begin{aligned} \dot{x} &= P_n^{-1} (\Lambda_n + \lambda_1^{(c)} I) P_n x \\ &+ P_c^{-1} \text{diag}(0, \lambda_2^{(c)} - \lambda_1^{(c)}, \dots, \lambda_{\dim(T)}^{(c)} - \lambda_1^{(c)}) P_c x \end{aligned} \quad (8)$$

Since $\mathcal{R}(\lambda_1^{(c)}) > 0$, it will influence the damping at least on one direction. Additionally, $\text{Tr}(T_c) = 0 = \sum_i \lambda_i^{(c)}$ in the proof suggests that the coupling will not change the sum of eigenvalues, but will influence their distribution, which inspires the following damping redistribution analysis.

B. Total Damping of Power Systems and Its Conservation

Damping is one of the critical stability properties associated with the real parts of eigenvalues of linear systems. It is natural to consider the sum of eigenvalues, which equals the sum of their real parts, as a measure of the total system damping.

Definition 2 (Total Damping). The total damping of a system \mathcal{G} is defined as

$$d_{\Sigma} \stackrel{\text{def}}{=} -\sum_i \lambda_i(T) \quad (9)$$

where T is the state matrix of the linearized system \mathcal{LG} defined in (6).

Recalling the relationship between eigenvalues and trace of a matrix, the total damping of \mathcal{G} can be expressed as follows:

$$d_{\Sigma} = -\text{Tr}(T) = \sum_{i \in \mathcal{V}} \left[\frac{d_i}{M_i} + \frac{1}{\tau_i} + \frac{1}{\tau_i} (r_i C_{1,ii} + g_i C_{2,ii}) \right] \quad (10)$$

where d_i/M_i is widely used as the metric of rotor-angle damping, and $1/\tau_i$ is essentially equivalent to the voltage damping (ratio) as defined in [29], [34].² Both terms reflect the damping provided by the devices, while the last two terms $C_{1,ii}$ and $C_{2,ii}$ suggest the impact related to the network strength. Roughly speaking, the stronger network connection (larger B_{ij}) will lead to larger $C_{1,ii}$ and $C_{2,ii}$, and so does d_{Σ} . Therefore, the definition is physically reasonable.

Now we investigate the conservation of the total damping. By simply employing the properties of matrix trace [16], we can derive the following equation (11). It indicates that the total damping does not change with or without consideration of angle-voltage coupling, which is referred to as its invariance.

$$d_{\Sigma} = -\sum_i \lambda_i = -\text{Tr}(T) = -\text{Tr}(T_n) = -\sum_i \lambda_i^{(n)} \quad (11)$$

This invariance reveals that angle-voltage coupling influences the stability by *redistributing* the total damping across the system, other than changing it. Specifically, the negative influence induced by the coupling essentially performs by redistributing the total damping in a more risky manner, as analyzed in Section IV.

C. Average Damping of Power Systems

Based on the concept of total damping, we further define the average damping as follows:

Definition 3 (Average Damping). The average damping of a system \mathcal{G} is defined as $d_{\text{ave}} \stackrel{\text{def}}{=} d_{\Sigma}/\dim(T)$, where d_{Σ} and T are the same as defined in the total damping.

An immediate result following this definition is that the average damping does not change with the angle-voltage coupling as the total damping invariant. Given the dimension of the system is fixed, the average damping also possesses the invariance property. Additionally, if let $d_{\text{ind},i} = -\mathcal{R}(\lambda_i(T))$ as the individual damping, then we have $d_{\text{ave}} \geq \min_i d_{\text{ind},i}$. The equation holds if and only if $d_{\text{ind},i} = d_{\text{ave}}$ for $i = 1, 2, \dots, \dim(T)$, which is the least dispersed damping distribution.

While total/average damping is invariant under coupling, it cannot assess stability risks from uneven redistribution induced by the angle-voltage coupling. The next section introduces the

²If further considering the exciter dynamics, the voltage damping can be adjustable. For example, it can be enhanced from $1/\tau_i$ to $(K_E + 1)/\tau_i$ if considering the exciter adopted in [19] with exciter gain K_E .

damping redistribution index κ to quantify this dispersion. Together with the total/average damping proposed in this section, we then formulate the damping redistribution mechanism.

IV. DAMPING REDISTRIBUTION MECHANISM OF ANGLE-VOLTAGE COUPLING

A. Damping Redistribution in SMIB Systems

Firstly, we illustrate the result in a traditional single-machine-infinite-bus (SMIB) system as shown in Fig.3(a). The phase-angle dynamics are assumed as (4) with $g_i = 0$. When the conditions of Lemma 1 satisfied, the eigenvalues $\lambda_1^{(n)}, \lambda_2^{(n)}$ of the non-coupling system T_n are

$$\lambda_1^{(n)} = -\frac{B_i V_i^* \cos \theta_i^* + \eta_i}{\zeta_i}, \lambda_2^{(n)} = -\frac{1 + r_i B_i}{\tau_i} \quad (12)$$

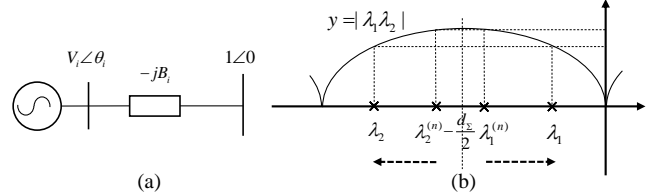


Fig. 3. Illustration of damping redistribution. (a): SMIB system. (b): eigenvalue distributions of the non-coupling system T_n and coupled system T .

As for the coupled system T , we can similarly obtain

$$\begin{aligned} \lambda^2 + \left(\frac{B_i V_i^* \cos \theta_i^* + \eta_i}{\zeta_i} + \frac{1 + r_i B_i}{\tau_i} \right) \lambda - \frac{r_i B_i^2 \sin^2 \theta_i^*}{\zeta_i \tau_i} \\ + \frac{B_i V_i^* \cos \theta_i^* + \eta_i}{\zeta_i} \cdot \frac{1 + r_i B_i}{\tau_i} = 0 \end{aligned} \quad (13)$$

It is easy to verify $-d_{\Sigma} = \lambda_1 + \lambda_2 = \lambda_1^{(n)} + \lambda_2^{(n)}$ by Vieta's formulas. Besides, it yields $\lambda_1 \lambda_2 - \lambda_1^{(n)} \lambda_2^{(n)} = -r_i B_i^2 \sin^2 \theta_i^* / \zeta_i \tau_i < 0$. As the eigenvalues λ_1, λ_2 are still real and symmetrical w.r.t. $x = -d_{\text{ave}} = -d_{\Sigma}/2$, their product always stays on the parabola $f(x) = -x(d_{\Sigma} + x)$, with or without the consideration of coupling. Therefore, the coupling-induced smaller product $\lambda_1 \lambda_2$ will force the eigenvalues away from the axis of symmetry, as shown in Fig.3(b).

The insight behind the simple case is that, as the total damping remains constant, the product of eigenvalues reflects their dispersion. From the perspective of average damping, the coupling influences stability by shifting the critical damping away from the average value. Specifically, in a stable system, a smaller product tends to result in a more dispersed distribution, thereby increasing the possibility of critical eigenvalues crossing the imaginary axis. Consequently, the system stability could be weakened, akin to the so-called *barrel effect*.

B. Damping Redistribution in Multi-inverter Systems

The above results can be extended to multi-inverter systems. It is interesting to see that, in multi-inverter systems, the eigenvalue shifts due to angle-voltage coupling are primarily parallel to the real axis, thereby preserving the applicability of insights from SMIB systems. Assuming uniform device parameters, this property can be elucidated as follows:

Theorem 1. Consider a system \mathcal{G} satisfying the conditions of Lemma 1. Suppose all eigenvalues of T_n are simple and all devices have identical parameters $(M_i, d_i, \tau_i, r_i, g_i)$. Letting $\{\lambda_i^{(n)}\}$ and $\{\lambda_i\}$ denote the spectrum of T_n and T , we have:

- $g = \mathbb{O}: \mathcal{I}(\lambda_i - \lambda_i^{(n)}) \rightarrow 0$ as T_c is sufficiently small.³
- $g \neq \mathbb{O}: \mathcal{I}(\lambda_i - \lambda_i^{(n)})/\mathcal{R}(\lambda_i - \lambda_i^{(n)}) \rightarrow 0$ as T_c and $\mathcal{A}^T V^*$ are sufficiently small.

Proof. The proof can be found in Appendix C of [31]. \square

The condition $\mathcal{A}^T V^* \approx \mathbb{O}$ in Theorem 1 implies that the directly connected buses have similar voltage amplitudes, which is usually satisfied with per-unit normalization. The uniform device dynamic parameter is a strong assumption. However, subsequent simulations confirm that the results also hold for more realistic non-uniform scenarios. Then, we prove the main results of the damping redistribution mechanism in multi-inverter systems.

Theorem 2. Consider a system \mathcal{G} satisfying the conditions of Lemma 1. Denote $\{\lambda_i^{(n)}\}$ and $\{\lambda_i\}$ as the spectrum of T_n and T . Then the following inequality holds

$$\left| \prod_i \lambda_i^{(n)} \right| \geq \left| \prod_i \lambda_i \right| \quad (14)$$

if one of the following conditions is satisfied:

- $g = \mathbb{O}: \|r\|_\infty/\lambda_{\min}(A) \leq \|D\|^{-1}$.
- $g \neq \mathbb{O}: \|r + g\|_\infty/\lambda_{\min}(A) \leq \|D\|^{-1}$, and both $\mathcal{A}^T V^*$ and Ψ are sufficiently small.

where the matrix Ψ is defined as

$$\Psi_{ij} = E_{ij} - D_{ij}^T = \begin{cases} \sum_{k \neq i} B_{ik} V_k^* (1 - V_i^*) \sin \theta_{ik}^* & \text{if } i = j \\ -B_{ij} V_i^* (1 - V_j^*) \sin \theta_{ij}^* & \text{if } i \neq j \end{cases} \quad (15)$$

Proof. The proof can be found in Appendix D of [31] as well as its alternative formulation. \square

The conditions of Theorem 2 are commonly satisfied in practice. Typically, a practical power system has $\|D\| \approx 10^1$ and $\lambda_{\min}(A) \approx 10^{0 \sim 1}$. When it comes to device parameters, for instance, SGs usually have $r_i = x_{di} - x'_{di} \approx 10^{-2}$, and the same applies to virtual-SGs. Additionally, the condition $\|g\|_\infty \approx 10^{-2 \sim -1}$ holds for most inverter-interfaced devices. The condition $\Psi \approx \mathbb{O}$ in the norm sense indicates the similarity of matrices E and D^T . In fact, its definition indicates the approximation is acceptable when $V_i^* \approx 1$ and $\theta_{ij}^* \approx 0$ for transmission grids. Furthermore, later simulations will suggest that the results still commonly hold even if these conditions are violated.

Noticing that the eigenvalue product equals its determinant, we define the ratio to reflect the damping redistribution strength.

Definition 4 (Damping Redistribution Index). The damping redistribution index is defined as

$$\kappa = |\det(T)/\det(T_n)| \quad (16)$$

³In this paper, a vector/matrix is called *small* if its any norm is small.

C. Interpretations of Trace-determinant Characterization

The previous section deploys the trace (total/average damping) and determinant of the state matrix to characterize the impact of phase-voltage coupling on power system stability. In the context of dynamic systems, the trace-determinant graph is a classic method to classify two-dimensional linear systems. We demonstrate that this method can be extended to higher-dimensional electrical power systems. Here, we further present the mathematical explanations to provide a better understanding of our result.

We start by introducing the geometric interpretation of total/average damping. Total damping quantifies a dynamic system's convergence rate between adjacent solution trajectories φ . As depicted in Fig.4, the volume of the infinitesimal perturbation hypersphere around trajectory $\varphi(t - \tau)$, denoted as $\delta V(t - \tau)$, is transformed into $\delta V(t)$ after evolving over time τ . Then, Liouville's formula indicates

$$\delta V(t)/\delta V(t - \tau) = \exp \left(\int_{t-\tau}^t \text{Tr}(T) ds \right) = \exp(-d_\Sigma \tau) \quad (17)$$

In other words, the total damping quantifies the exponential convergence rate of trajectories in phase space, thereby reflecting the structural stability. The result also generalizes nonlinear system models if the damping is generalized based on Lyapunov exponents. With this extension, the total damping d_Σ also stays invariant even though individual dampings d_i change over time for the scenarios $g = \mathbb{O}$. Readers interested in a deeper exploration may refer to [29], [35].

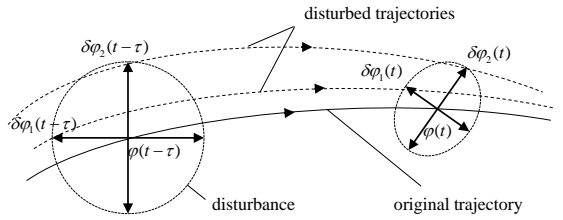


Fig. 4. Geometric interpretation of total damping in phase space.

Furthermore, the damping redistribution index also directly connects with the stability and dynamic performance of the system. Omitting the individual damping provided by complex eigenvalues, as subsequent simulations suggest they hardly change under the coupling, the following results can be derived:

- Since $\det(T) = \prod_i \lambda_i$, it is easy to check that $|\det(T)/\det(T_n)| = 0$ if and only if there exists a eigenvalue $\lambda = 0$, which directly suggests instability.
- Assume the coupling only shifts the real eigenvalues parallel to the real axis, as indicated in Theorem 1. Then $|\det(T)/\det(T_n)|$ is maximized if and only if all individual dampings are identical, i.e., $\min_i d_{\text{ind},i} = d_{\text{ave}}$.
- The stability criteria for the system in the presence of $g = \mathbb{O}$ in [12] and Chapter 2 of [34] can be easily derived from our framework by combining Lemma 1 of [12] and the proof of Theorem 2 when $|\det(T)| = 0$, as formally demonstrated by Corollary 1.

Corollary 1. A system \mathcal{G} with $g = \mathbb{O}$ is stable if and only if one of the following two sets is satisfied

$$\begin{aligned} & \underbrace{A}_{\text{angle-related}} \succ 0, \quad \underbrace{r^{-1} + C_1 - D^T A^{-1} D}_{\text{voltage-related coupling term}} \succ 0 \\ & \underbrace{r^{-1} + C_1}_{\text{voltage}} \succ 0, \quad \underbrace{A}_{\text{angle-related}} - \underbrace{D(r^{-1} + C_1)^{-1} D^T}_{\text{coupling term}} \succ 0 \end{aligned} \quad (18)$$

Therefore, maintaining the determinant away from zero benefits stability. Moreover, a larger determinant index usually implies better dynamic performance as the critical damping $\min_i d_{\text{ind},i}$ determines the slowest mode. Intuitively, the ratio $|\det(T)/\det(T_n)|$ could quantify the critical eigenvalue shift under the impact of coupling, as confirmed in Section VI and Appendix I of [31].

Remark 4. In a pure mathematical context, a decrease in κ , signifying a diminution of the product of all eigenvalues, does not conclusively ensure that the rightmost eigenvalue moves closer to the imaginary axis. Besides, we clarify that κ serves as an effective metric of damping redistribution trends for power system models. Firstly, the critical value where index κ turns from positive to zero corresponds exactly to the point where an eigenvalue crosses the imaginary axis, as we just demonstrated. Secondly, later numerical analysis in Section VI-B shows that a smaller κ correlates strongly with rightward shifts in the rightmost eigenvalue in a nearly linear manner. Therefore, although κ does not deterministically force rightward movement, it is a highly reliable *statistical predictor* of such shifts in practical power systems.

D. Extension to Including First-order Phase-angle Dynamics

This part extends the proposed method to systems that include first-order phase-angle dynamics (4). By setting $\zeta_i = \tau_{\text{dpP},i}/D_{\text{dpP},i}$ and $\eta_i = 1/D_{\text{dpP},i}$, the first-order phase-angle model can represent $P - \theta$ droop-controlled inverters. It can also represent $P - f$ droop-controlled inverters and dynamic loads in the structure-preserving model [36] by setting $\eta_i = 0$. Commonly, the parameters $\zeta_i, \eta_i \geq 0$ hold in practice.

Consider the set of devices in this system as $\mathcal{V}' = \mathcal{V}'_1 \cup \mathcal{V}'_2$, where devices with the phase-angle dynamics satisfying (2) and (4) belong to \mathcal{V}'_1 and \mathcal{V}'_2 , respectively. Then the dynamics of the extended system $\mathcal{G}' = \tilde{G}(\mathcal{V}', \mathcal{E}')$ can be represented by the state matrix $T' = T'_\theta + T'_c$ similar to (7), in terms of the states $[\Delta\theta_{\mathcal{V}'_1}^T, \Delta\omega_{\mathcal{V}'_1}^T, \Delta\theta_{\mathcal{V}'_2}^T, \Delta V^T]^T$. The sub-matrices are defined as follows:

$$\begin{aligned} T'_\theta &= \begin{bmatrix} \mathbb{O} & I & \mathbb{O} \\ -M^{-1}A_{\mathcal{V}'_1 \times \mathcal{V}'_1} & -M^{-1}d & -M^{-1}A_{\mathcal{V}'_1 \times \mathcal{V}'_2} \\ -\zeta^{-1}A_{\mathcal{V}'_2 \times \mathcal{V}'_1} & \mathbb{O} & -\zeta^{-1}(A_{\mathcal{V}'_2 \times \mathcal{V}'_2} + \eta) \end{bmatrix} \\ T'_{\theta V} &= [\mathbb{O} \quad (-M^{-1}D_{\mathcal{V}'_1 \times \mathcal{V}'})^T \quad (-\zeta^{-1}D_{\mathcal{V}'_2 \times \mathcal{V}'})^T]^T \\ T'_{V\theta} &= [-\tau^{-1}(rD^T + gE)_{\mathcal{V}' \times \mathcal{V}'_1} \quad \mathbb{O} \quad -\tau^{-1}(rD^T + gE)_{\mathcal{V}' \times \mathcal{V}'_2}] \\ T'_V &= -\tau^{-1}(rC_1 + gC_2 + I) \end{aligned} \quad (19)$$

For this system, the total damping is written as

$$d'_\Sigma = d_\Sigma + \sum_{i \in \mathcal{V}'_2} \left[\frac{1}{\zeta_i} (\eta_i + A_{ii}) \right] \quad (20)$$

where d_Σ has been given in (10). The above equation suggests that for first-order phase-angle devices, faster dynamics (smaller ζ_i), stronger droop strength (larger η_i), and tighter connection in the corresponding region (larger A_{ii} for $i \in \mathcal{V}'_2$) all benefit the total damping. Then we examine its well-posedness conditions and the redistribution theorem in order.

Lemma 3. For the system \mathcal{G}' , the matrices T'_θ and T'_V are Hurwitz on D_f if the conditions of Lemma 1 are satisfied.

Proof. The proof can be found in Appendix E of [31]. \square

Theorem 3. Given a system \mathcal{G}' satisfying the conditions of Lemma 1, then the statements of Theorem 2 still hold for eigenvalues of T' and T'_n , if replacing A with A' defined as

$$A' \stackrel{\text{def}}{=} A + \text{diag}(\mathbb{O}, \eta) = \begin{bmatrix} A_{\mathcal{V}'_1 \times \mathcal{V}'_1} & A_{\mathcal{V}'_1 \times \mathcal{V}'_2} \\ A_{\mathcal{V}'_2 \times \mathcal{V}'_1} & A_{\mathcal{V}'_2 \times \mathcal{V}'_2} + \eta \end{bmatrix} \quad (21)$$

Proof. The proof can be found in Appendix F of [31]. \square

Apart from the similar physical interpretation as that of Theorem 2, this theorem further indicates that the damping dispersion shrinks with a larger droop strength (larger η_i) for the system containing $P - f$ droop inverters, which facilitates the system stability.

In brief, building on Section III's key insight—that angle-voltage coupling conserves total damping d_Σ but not its distribution—we now prove that coupling redistributes damping dispersively and its strength can be quantified by the redistribution index κ .

V. DAMPING-REDISTRIBUTION-BASED ANALYSIS OF ANGLE-VOLTAGE COUPLING

This section employs the proposed damping-redistribution methodology to analyze the angle-voltage coupled stability. Firstly, it is analyzed how various factors, such as device parameters and number, network connection, and control strategies, influence the angle-voltage coupling strength with the proposed indices. Moreover, a comparison between the proposed methodology and existing literature is also demonstrated. For brevity, the analysis is based on the system \mathcal{G} since the result can be naturally extended to \mathcal{G}' .

A. On the Influence of Device's Parameters and Network's Power Flow on Angle-Voltage Coupling

Both device dynamic parameters and network power flow influence the total/average damping as shown in (10). Therefore, the analysis focuses on the factors affecting the damping redistribution. The proof of Theorem 2, see Appendix D indicates the following term provides a positively correlated metric of the dispersion of total damping

$$\|r + g\|_\infty \cdot \|D\|/\lambda_{\min}(A) \quad (22)$$

Noticing $\mathbb{1}$ has been excluded from D_f , the term $\lambda_{\min}(A) \neq 0$ represents the algebraic connection strength of a network [36] and $\|D\|$ reflects the angle-voltage coupling induced by the power flow. The terms r and g are parameters of the device voltage control. According to (22), strengthening network connection strength (larger $\lambda_{\min}(A)$) or device voltage control

(smaller r or g) can reduce the dispersion of the total damping (larger $|\det(T)/\det(T_n)|$), and vice versa. In this sense, (22) provides a quantitative explanation of how power flow, network connection, and device controls combine to influence system stability by redistributing the total/average damping.

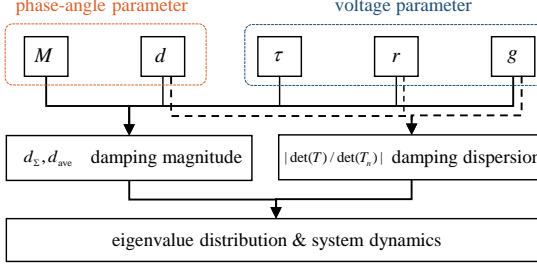


Fig. 5. Approaches of device dynamic parameters to influence dynamics.

Remark 5. An interesting observation is that the device parameters influence the dynamics from different approaches, as illustrated in Fig. 5. While all parameters influence the total/average damping, the time constants M and τ do not impact damping dispersion as quantified by the determinant index. This fact has been mathematically justified in the proof of Theorem 2, in which both $\det(T), \det(T_n) \propto \det(M^{-1}) \cdot \det(\tau^{-1})$ and thus eliminated in fraction $|\det(T)/\det(T_n)|$.

B. On the Influence of Number of Integrated Devices on Angle-Voltage Coupling

In this section, we will explore the potential impact of increasing the number of devices on the strength of the coupling and, consequently, the system stability, even when the system's operating conditions remain unchanged. For example, a single SG in Fig. 6(a) is replaced by multiple parallel inverters in Fig. 6(b). The steady-state power output remains consistent before and after the replacement, and it is equally distributed among the inverters. This substitution exemplifies the shift from a few conventional synchronous generators to massive renewable energy sources.

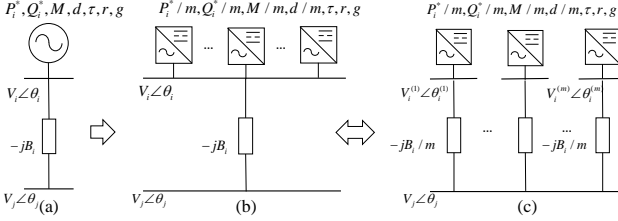


Fig. 6. Replacement and equivalence of integrated devices. (a): original i -th device (a single SG). (b): replaced devices integrated on i -th bus (m inverters in total). (c): an equivalent transformation of (b) from the perspective of external port characteristics.

In our analysis, we use the inverter subsystem in Fig. 6(c) for computational simplicity. Here the common line is evenly split into m lines, hence the two subsystems are equivalent from the perspective of external port characteristics. We emphasize that this equivalence is solely for mathematical modeling and does not imply the actual splitting of lines.

1) *Total and average damping.* For the system with each source uniformly replaced by m inverters, the total damping $d_{\Sigma}^{(m)}$ can be computed as follows

$$\begin{aligned} d_{\Sigma}^{(m)} &= \sum_{i=1}^n \sum_{k=1}^m \left[\frac{d_i/m}{M_i/m} + \frac{1}{\tau_i} (1 + r_i C_{1,ii}^{(m)} + g_i C_{2,ii}^{(m)}) \right] \\ &\approx m \sum_{i=1}^n \left[\frac{d_i}{M_i} + \frac{1}{\tau_i} (1 + r_i \frac{C_{1,ii}^{(1)}}{m} + g_i \frac{C_{2,ii}^{(1)}}{m}) \right] \end{aligned} \quad (23)$$

where $C_{1,ii}^{(m)}$ and $C_{2,ii}^{(m)}$ denote the terms with each source replaced by m inverters. The relationships $C_{1,ii}^{(m)} = C_{1,ii}^{(1)}/m$ and $C_{2,ii}^{(m)} \approx C_{2,ii}^{(1)}/m$ hold because of $B_{ii}^{(m)} = B_{ii}^{(1)}/m$ (see the definitions of $C_{1,ii}$ and $C_{2,ii}$).⁴ While the total damping is divergent with $m \rightarrow \infty$, the average damping satisfies

$$\begin{aligned} d_{\text{ave}}^{(m)} &= d_{\Sigma}^{(m)} / (m \dim(T)) \\ &\approx \frac{1}{\dim(T)} \sum_{i=1}^n \left[\frac{d_i}{M_i} + \frac{1}{\tau_i} (1 + r_i \frac{C_{1,ii}^{(1)}}{m} + g_i \frac{C_{2,ii}^{(1)}}{m}) \right] \\ &\leq \frac{1}{\dim(T)} \sum_{i=1}^n \left[\frac{d_i}{M_i} + \frac{1}{\tau_i} (1 + r_i C_{1,ii}^{(1)} + g_i C_{2,ii}^{(1)}) \right] = d_{\text{ave}}^{(1)} \end{aligned} \quad (24)$$

The above inequality indicates that increasing device number m will reduce the average damping when m is large enough.

2) *Damping redistribution.* From the perspective of external port characteristics, the i -th bus has the aggregate parameters $(M, d, r/m, g/m)$. Hence a larger device number m gives a less dispersed damping distribution, as (22) suggests.

In brief, integrating more inverters can reduce the average damping, but meanwhile, shrink the damping distribution. The two aspects basically have opposite effects on the coupled stability, and the dominant factor depends on the specific systems. This issue will be further analyzed in the simulation.

C. Regulating Angle-voltage Coupling via Cross-loop Control

This paper suggests the stability of coupled systems can be enhanced generally through two approaches from the damping perspective: A direct approach is to improve the stability of each subsystem of T_n , implemented by strengthening device control such as d, r and g in (2). Alternatively, as the coupling is inevitable, adjusting the damping distribution through the coupling T_c provides an additional approach. This can be implemented by adding voltage/frequency feedback into frequency/voltage control loops, respectively, referred to as cross-loop control.

Consider the following cross-loop-controlled device dynamics (25) and denote the corresponding system as \mathcal{G}'' . Clearly, the cross-loop control influences neither the equilibrium nor

⁴The latter approximation cannot be equation since $C_{2,ii}^{(m)}$ is also determined by θ_i^* and V_i^* apart from B_{ii} (see its definition). Since integrating more inverters might slightly adjust the steady point, the term might change with m . However, the influence is bounded since $|\cos \theta_{ij}| \leq 1$ and V_i^* approaches its setting value as $m \rightarrow \infty$. Therefore, the approximation does not essentially change our analysis in the limit process.

the total damping. Besides, it degenerates to the original dynamics (2) if $K_{\omega V,i} = K_{V\theta,i} = K_{V\omega,i} = 0$.

$$\begin{aligned}\dot{\theta}_i &= \omega_i \\ M_i \dot{\omega}_i &= -d_i \omega_i - P_i + P_{mi} - K_{\omega V,i}(V_i - V_i^*) \\ \tau_i \dot{V}_i &= -V_i + u_i - r_i \frac{Q_i}{V_i} - g_i Q_i - K_{V\theta,i} \int \omega_i dt - K_{V\omega,i} \omega_i\end{aligned}\quad (25)$$

Here, we note that the proposed cross-loop control provides a uniform model of some existing methods, such as:

- For SGs, the voltage-related feedback can be viewed as the extreme approximation of the PSS controllers. As for inverters, the PI feedback of ω_i can represent the voltage-based frequency controllers proposed in [25]. The coupling compensation through cross-loop droop control [37] also satisfies this form.
- The combined frequency-voltage control of distributed energy resources [27], derived from the static power flow equation, can be transformed by properly choosing $V - P$ and $\omega - Q$ feedback PI parameters.
- It can be viewed as the small-signal degeneration for the dynamic power compensation strategy [23], where the feedback $K_{V\theta}$ and $K_{\theta V}$ are no longer diagonal.

The state matrix of the linearized system \mathcal{G}'' is denoted as T'' , written as

$$\left[\begin{array}{c|c} \emptyset & I \\ \hline -M^{-1}A & -M^{-1}d \\ -\tau^{-1}(rD^T + gE + K_{V\theta}) & -\tau^{-1}K_{V\omega} \\ \hline -\tau^{-1}(rC_1 + gC_2 + I) & -\tau^{-1}(rC_1 + gC_2 + I) \end{array} \right] \quad (26)$$

The damping dispersion of T'' is quantified by the determinant ratio $|\det(T'')/\det(T_n'')|$. Therefore, increasing the ratio via appropriate cross-loop control can facilitate stability. We denote by J the Jacobi matrix of the extended power flow, and by K_{cl} the cross-loop control matrix, which are

$$J \stackrel{\text{def}}{=} \begin{bmatrix} A & D \\ rD^T + gE & rC_1 + gC_2 + I \end{bmatrix}, K_{cl} \stackrel{\text{def}}{=} \begin{bmatrix} \emptyset & K_{\omega V} \\ K_{V\theta} & \emptyset \end{bmatrix} \quad (27)$$

For simplification, we consider the situation that the cross-loop control parameters are uniformly scaled on the basis of an initial $K_{cl}^{(0)}$, i.e., $K_{cl} = \sigma K_{cl}^{(0)}$. Despite the difficulty of solving an optimal K_{cl} , the following theorem shows there generally exists at least one cross-loop control to enhance stability, which explains the effectiveness of previous cross-loop controls from the perspective of damping redistribution.

Theorem 4. Suppose the conditions of Lemma 1 hold for the system \mathcal{G}'' . If $\det(J) > 0$ and $\text{Tr}(J^{-1}K_{cl}^{(0)}) \neq 0$ for a given $K_{cl}^{(0)}$, then there exists at least one σ_0 and corresponding control $K_{cl} = \sigma_0 K_{cl}^{(0)}$ such that $|\det(T'')/\det(T)| > 1$.

Proof. The proof can be found in Appendix G of [31]. \square

Remark 6 (Physical Interpretation of Cross-Loop Control). While cross-loop control formally introduces $P-Q$ coupling in device dynamics, we note that *effective $P-Q$ decoupling can be only achieved by cross-loop control*, although it sounds a little counterintuitive. Consider the power flow equations (28),

which lead to inevitably angle-voltage coupling dynamics via D and D^T (and also E).

$$\begin{aligned}\Delta P &= A\Delta\theta + D\Delta V, \\ \Delta \frac{Q}{V} &= D^T\Delta\theta + C_2\Delta V \text{ or } \Delta Q = E\Delta\theta + C_1\Delta V\end{aligned}\quad (28)$$

Clearly, this power-flow-induced coupling cannot be eliminated if considering the decoupled device controls (i.e., θ/ω regulated solely by P , and V solely by Q). Therefore, achieving decoupling of phase-angle and voltage dynamics *must rely on* cross-loop control, which is also suggested by (26). This aligns with power electronics literature, where cross-loop signals are essential to $P-Q$ decoupling techniques [3], [33].

Moreover, the prototype provides a useful insight into stability enhancement *beyond decoupling*: The coupling worsens the stability by redistributing the total damping more dispersively compared to the non-coupled system, as illustrated in Fig.3(b). Previous works, such as virtual impedance, aimed to recover the non-coupled dynamics through decomposition controls, i.e., let λ_1 approach $\lambda_1^{(n)}$ in Fig.3(b). However, this paper indicates that it is possible to achieve even better dynamics than the non-coupled ones with a more concentrated damping distribution by proper cross-loop controllers, i.e., move λ_1 to the left of $\lambda_1^{(n)}$ without violating the damping conservation, which is our further research direction.

D. Comparison with Existing Methods

The proposed mechanism introduces a fundamentally novel perspective for analyzing angle-voltage coupling by establishing the damping redistribution mechanism as the universal destabilizing pathway in inverter-dominant systems. Unlike prior works, the proposed damping redistribution mechanism provides a unified framework applicable to heterogeneous grids integrating SGs and diverse inverters. Moreover, it holistically captures critical dynamic features—including device-specific damping effects and multi-device interactions—yielding a more comprehensive stability description than existing methods. These characteristics are summarized in Table.I.

VI. CASE STUDY

A heterogeneous IEEE 39-bus system integrated as shown in Fig.7 is used for verification. The tested system is integrated with massive inverter-based resources, including the widely used VSG-controlled and droop-controlled GFM devices, and also GFL devices. The detailed configurations can be found in Appendix H of [31]. All data and codes to generate the results in this paper have been open-sourced on <https://github.com/lingo01/DampingRedistribution>.

Validation Method: All simulations demonstrate how angle-voltage coupling undermines stability by redistributing damping dispersively. Concretely: (i) Fig.8 proves coupling reduces critical damping via rightward eigenvalue shifts; (ii) Fig.9 and Table.II show that κ serves as a quantification of coupled instability risk under various systems and operation situations; (iii) Fig.11 verifies κ -maximizing controls mitigate coupling impacts.

TABLE I
COMPARISON OF DIFFERENT METHODS TO ANALYZE THE COUPLING'S IMPACT

Method	Foundation	Model applicability	Applicable to transmission grid	Capture device damping dynamics	Quantifies coupling severity
Proposed	eigenvalue theory (overall distribution)	SG & inverter	✓	✓	✓
Eigenvalue-estimation-based [12], [14]	eigenvalue theory (estimate critical one)	SG	✓		✓
Energy-function-based [19]	Lyapunov theory	SG & inverter	✓		
Transfer-function-based [3]	Laplace transformation	SG & inverter		✓	

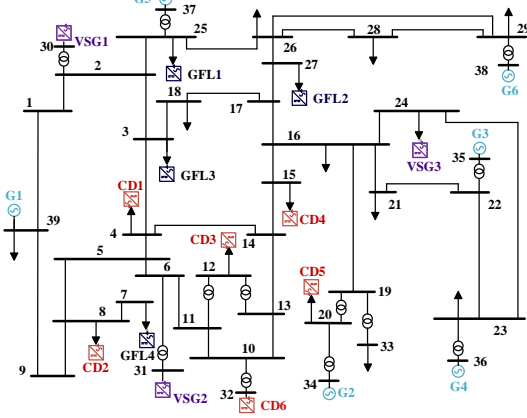


Fig. 7. A heterogeneous IEEE 39-bus system with inverter-interfaced devices including SGs, constant power loads, GFL inverters, and GFM inverters($P - f/Q - V$ conventional-droop-controlled and VSG-controlled inverters).

A. Eigenvalue Distribution Characteristics

Fig.8 illustrates the rightmost eigenvalue distributions under different operation situations. Compared to the non-coupling system T_n , the actual system T generally has the following characteristics: Firstly, the coupling shifts the real rightmost eigenvalues to the right side, leading to less damping. For example, the rightmost eigenvalue shifts rightward under coupling from -0.1303 to -0.0710 in Fig.8(d), which suggests a 45.51% decrease in stability margin. Secondly, the complex ones generally do not move. Even if they move to the left, the amplitude is relatively small. Lastly, the non-rightmost eigenvalues, which are not drawn in the figure, move left to balance the invariant total damping. Generally, the distribution of eigenvalues is more dispersed under the influence of coupling. The influence of specific factors is noted in the following aspects: Heavier load, weaker device voltage control strength, and slower voltage dynamics will shift the rightmost eigenvalues closer to the imaginary axis as indicated by Fig.8(a)-(d), (e)-(h) and (i)-(l) respectively. All these facts align with our analysis in Section IV.

B. Redistribution Characteristics

The part analyzes the overall eigenvalue dispersion induced by the coupling. The ratio $|\det(T)/\det(T_n)|$ w.r.t. the scaling ρ_{load} , ρ_{net} , $\gamma_{r,g}$ and γ_τ is shown in Fig.9(a)-(d). Firstly, the result of Theorem 2 holds even beyond its conditions. Generally, practical devices have sufficiently small voltage parameters r and g to satisfy the conditions of the theorem.

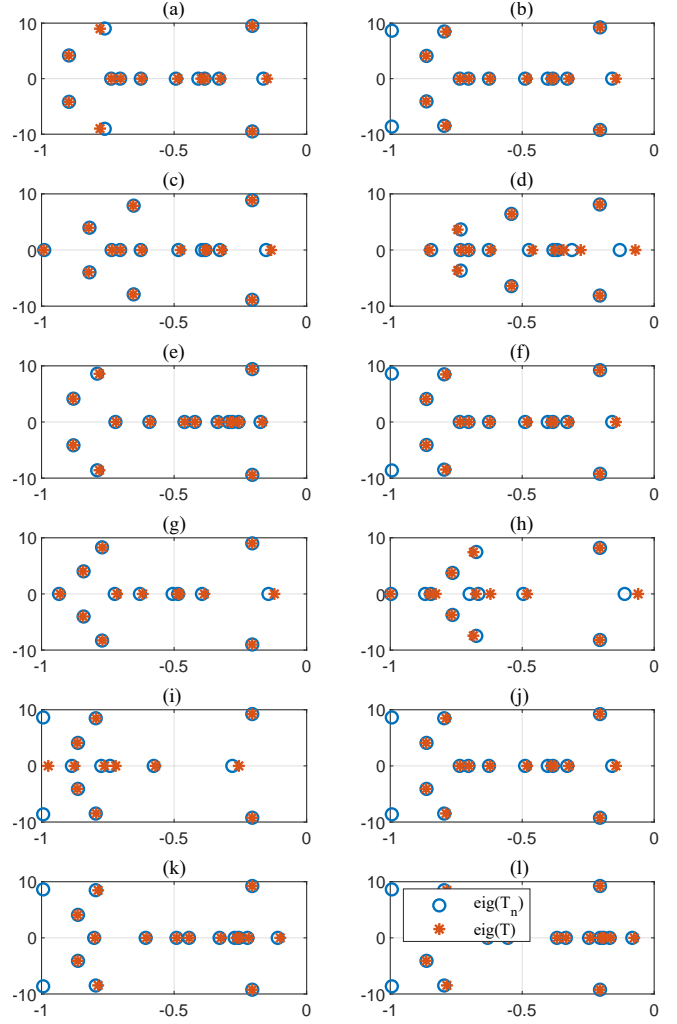


Fig. 8. Rightmost eigenvalue distributions with/without consideration of coupling. (a)-(d): static loads are uniformly scaled with $(P_{set}, Q_{set}) = \rho_{load}(P_{set}^{(0)}, Q_{set}^{(0)})$, $\rho_{load} = 0.5, 1.0, 1.5, 2.0$ in order. (e)-(h): device voltage control parameters are uniformly scaled with $(r, g) = \gamma_{r,g}(r^{(0)}, g^{(0)})$, $\gamma_{r,g} = 0.5, 1.0, 1.5, 2.5$. (i)-(l): device voltage time constants are uniformly scaled with $\tau = \gamma_\tau \tau^{(0)}$, $\gamma_\tau = 0.5, 1.0, 1.5, 2.0$.

However, if any constant power sources or connecting buses are integrated into the system, their models with $g \approx \infty$ make it almost impossible to meet the conditions. Whereas, $|\det(T)/\det(T_n)| < 1$ still holds in all figures, indicating its common effectiveness. Besides, the result also holds for various benchmark systems, as shown in Table.II. It demonstrates that $\kappa < 1$ holds universally across systems from 4 to 500 buses, empirically validating that the impact of angle-voltage

coupling widely exists in practice power systems and thus requires careful consideration.⁵ Further theoretical analysis can be found in Appendix I of [31].

TABLE II
DETERMINANT RATIO FOR DIFFERENT TEST SYSTEMS

case name	4gs	9	39	118	ACTIVSg200
$ \det(T)/\det(T_n) $	0.986	0.966	0.764	0.400	0.716
case name	6ww	30	57	145	ACTIVSg500
$ \det(T)/\det(T_n) $	0.962	0.976	0.633	0.606	0.612

Fig.9(a)-(d) indicates $|\det(T)/\det(T_n)|$ is negatively correlated with $\|T_c\|_F/\|T\|_F$, but more sensitive to the eigenvalue shift. Additionally, the following results are worth noting:

- Fig.9(a) suggests heavier load leads to a more dispersed distribution of eigenvalues (smaller $|\det(T)/\det(T_n)|$), which aligns with the eigenvalue analysis in Fig.8(a)-(d).
- A strong network connection can reduce the dispersion of the total damping, as suggested by Fig.9(b). A sufficiently strong network $\rho_{\text{net}} > 3$ can even approximately eliminate the impact of the coupling.
- Since r^{-1} and g^{-1} respectively represent the control strength of var-current and reactive power, Fig.9(c) indicates that the weaker control (larger $\gamma_{r,g}$) leads to a more dispersed damping distribution.
- $|\det(T)/\det(T_n)|$ does not change with the voltage timescale γ_τ as depicted in Fig.9(d). However, it does not indicate the invalidation of the proposed mechanism. As explained in Section V, despite the unchanged overall redistribution, reducing τ_i increases the voltage-related term $1/\tau_i$ in (10), enhancing total damping d_Σ and also the stability margin, which is also supported by the actual eigenvalue shifts in Fig.8(i)-(l). This contrasts with d_Σ 's effect on response speed: larger d_Σ accelerates settling times. Here, $1/\tau_i$ is the intrinsic damping coefficient of voltage dynamics, akin to d_i/M_i for angle dynamics as we explained in Section III-B.

The redistribution index can also help analyze how the integration of renewable energy sources (RESs) affects system stability characteristics. Assuming RESs are integrated in a GFL manner, their penetration level related to $|\det(T)/\det(T_n)|$ is shown in Fig.9(e). The figure indicates that increasing GFL penetration leads to more severe coupling. Moreover, depending on the alternative replacement order, the determinant ratio falls below 0.4 with the corresponding penetration level varied widely between 50% and 90%. The result also suggests $|\det(T)/\det(T_n)| = 0.4$ may serve as a threshold for distinguishing strongly and weakly coupled systems. When falling below it, the coupling-induced rightward shift of the critical eigenvalue usually exceeds 0.05, or 40%, compared to the non-coupled system. For these situations, it might be necessary to consider the coupling in stability analysis. On the contrary, a higher value indicates that the error of traditional decoupled analysis methods is acceptable.

Among all dampings, the critical one related to the rightmost eigenvalue dominates stability. Fig.9(f) and (g) suggest

⁵Parameters are derived from the MATPOWER database. For example, the case name 4gs corresponds to benchmark *case4gs* in MATPOWER.

$|\det(T)/\det(T_n)|$ also serves as a metric of its movement. Although both $\max \mathcal{R}(\lambda^{(n)})$ and $\max \mathcal{R}(\lambda)$ present a nonlinear relationship with $|\det(T)/\det(T_n)|$, it is dramatic that $\max \mathcal{R}(\lambda) - \max \mathcal{R}(\lambda^{(n)})$, indicating the movement induced by the coupling, is approximately linearly correlated with $|\det(T)/\det(T_n)|$ with approximated slope $1/\max \mathcal{R}(\lambda^{(n)})$. Theoretical explanations can be found in Appendix I of [31]. Generally, Fig.9(g) unifies the coupling instability mechanisms. The nearly linear trend $\max \mathcal{R}(\lambda) - \max \mathcal{R}(\lambda^{(n)}) \approx -\kappa / \max \mathcal{R}(\lambda^{(n)})$ proves that κ directly measures critical damping loss. At $\kappa < 0.4$, eigenvalue shifts exceed 40%, necessitating coupled modeling. Conversely, $\kappa > 0.8$ implies shifts below 5%, permitting traditional decoupled analysis.

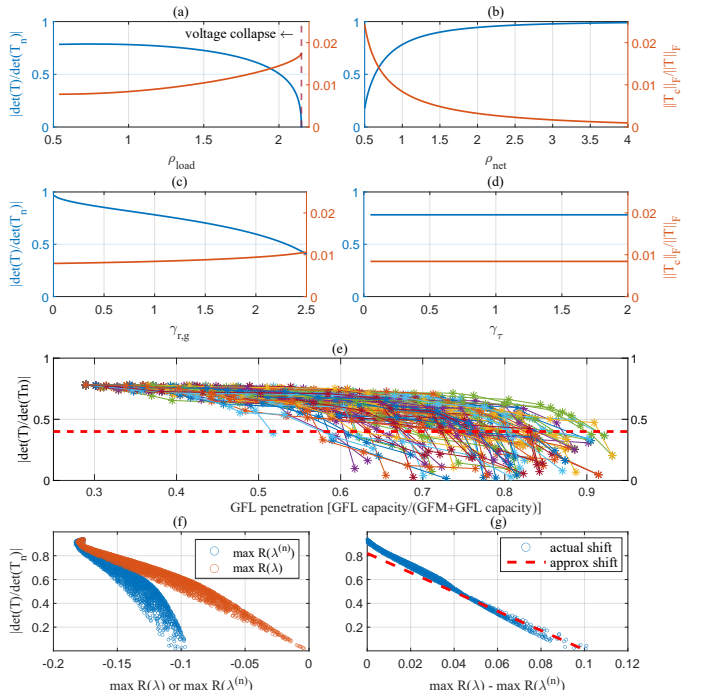


Fig. 9. Changes of $|\det(T)/\det(T_n)|$ and $\|T_c\|_F/\|T\|_F$. (a): with load scaling factor ρ_{load} . (b): with network scaling factor ρ_{net} ($B = \rho_{\text{net}} B^{(0)}$). (c): with voltage control parameter scaling factor $\gamma_{r,g}$. (d): with voltage time constant scaling factor γ_τ . (e): with GFL penetration. GFM devices are replaced one by one with the same steady power until the system is unsolvable or unstable. There are different replacement orders, but only 100 approaches are present here for clarity. (f) and (g): with the maximum eigenvalue of the non-coupled system T_n ($\max \mathcal{R}(\lambda^{(n)})$), coupled system T ($\max \mathcal{R}(\lambda)$), and their difference. Here 10,000 samplings are presented with all scaling factors randomly selected from $\rho_{\text{load}} \in (0.5, 2.15)$, $\rho_{\text{net}} \in (0.5, 4.0)$, $\gamma_{r,g} \in (0.005, 2.5)$ and $\gamma_\tau \in (0.05, 2.0)$ uniformly. The slope of the dashed line in (g) is $1/\langle \max(\lambda^{(n)}) \rangle$, which corresponds to the system with all scaling factors adopting their average value in the range.

C. Impact of the Number of Integrated Devices

Fig.10 shows the variation in damping distribution as the inverter number n_{total} changes, replacing with the approach described in Section V-B. Fig.10(a) and (b) respectively display the changes in total damping d_Σ and average damping d_{ave} . Consistent with the theoretical analysis presented in Section V-B, increasing n_{total} leads to a decline in average damping, despite the increase in total damping. This pattern holds irrespective of whether power sources are replaced uniformly or

non-uniformly. Meanwhile, Fig.10(c) indicates that integrating more devices can also shrink the dispersion of the damping distribution. Specifically, the damping redistribution index κ increases from 0.8128 to 1.000 when the integration number increases from 15 to 1000. Indeed, the rightmost eigenvalue distributions in Fig.10(d) and (e) corroborate this observation. As the device number increases, the eigenvalue movement induced by the damping redistribution decreases, while the smaller average damping forces all eigenvalues to move closer to the imaginary axis. Generally, the damping redistribution has a more significant influence as the total/average damping is usually sufficiently large.

This fact is supported by the increase in the actual critical damping in the test system. Specifically, the critical eigenvalues $\max \mathcal{R}(\lambda)$ are -0.1473 ($n_{\text{total}}=15$) and -0.1716 ($n_{\text{total}}=1000$), while $\max \mathcal{R}(\lambda^{(n)})$ are -0.1613 ($n_{\text{total}}=15$) and -0.1716 ($n_{\text{total}}=1000$), respectively. Firstly, the critical eigenvalue of the coupled system $\max \mathcal{R}(\lambda)$ moves left, which suggests an increased stability margin. Secondly, the difference between the coupled and the non-coupled systems $\max \mathcal{R}(\lambda) - \max \mathcal{R}(\lambda^{(n)})$ is smaller with more devices integrated, which indicates that integrating more devices decreases the impact of coupling.

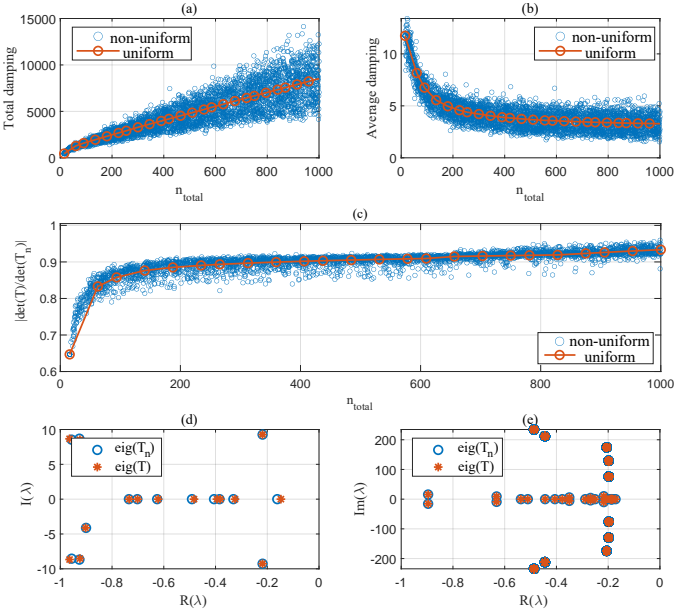


Fig. 10. (a), (b), and (c): Relationships of total damping d_{Σ} , average damping d_{ave} , and determinant ratio $|\det(T)/\det(T_n)|$ with the total number of integrated inverters n_{total} . The red line represents each device is uniformly replaced by the same number of inverters, while the blue points represent non-uniform replacements. In the non-uniform replacement method, the selection of substituting inverters follows a uniform distribution with 10,000 random samplings. (d) and (e): the eigenvalue distributions for $n_{\text{total}} = 15$ and $n_{\text{total}} = 1000$ when inverters are integrated uniformly, respectively.

D. Stability Enhancement through Cross-loop Control

Fig.11 has verified the effectiveness of the cross-loop control. Fig.11(a) indicates that there does exist some $\sigma > 0$ such that $|\det(T'')/\det(T)| > 1$, denoted by the cyan region. In this region, the cross-loop control allocates the total damping in a

less dispersed manner, hence it is more beneficial for system stability. Besides, as confirmed by Fig.11(b), the most critical damping – $\max \mathcal{R}(\lambda)$ is larger with increasing σ in the region. Moreover, except for a pair of complex eigenvalues ② and ③ slightly moving to the right, all displayed eigenvalues move away from the imaginary axis, as indicated by Fig.11(c) and (d), thus verifying the above analysis.

Furthermore, the simulations also indicate the necessity of considering the total damping. If only aiming to minimize $\max \mathcal{R}(\lambda)$, $\sigma \approx 0.8$ is desired. However, in this situation, the complex eigenvalues ② and ③ replace ① to be the most critical ones and worsen the stability. Contrary to the critical eigenvalue perspective, the determinant index precisely captures the fact as shown by the less $|\det(T'')/\det(T)|$ at $\sigma \approx 0.8$ compared to $\sigma = 0.2$, thereby providing an alternative and overall perspective to quantify the stability.

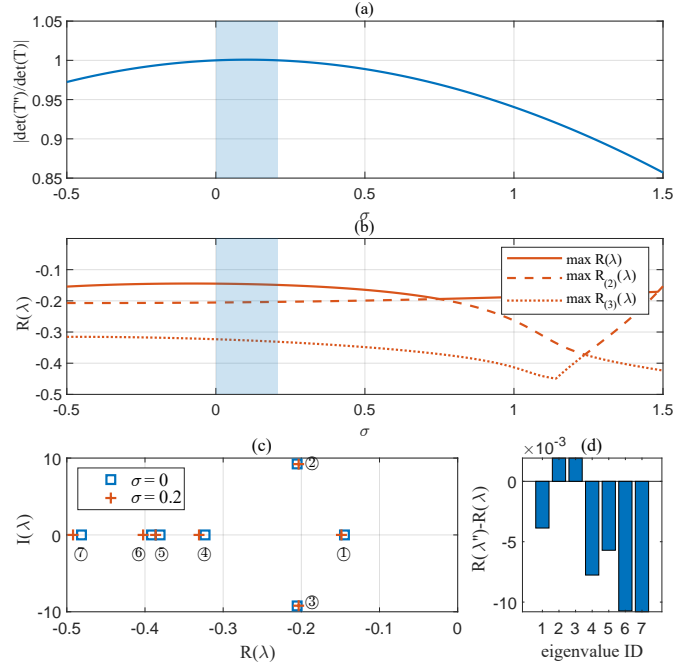


Fig. 11. Damping redistribution with cross-loop control scaling σ . The initial control is selected as $(K_{\omega V, \mathcal{V}_1''}^{(0)}, K_{\theta V, \mathcal{V}_2''}^{(0)}, K_{V\theta, \mathcal{V}_1''}^{(0)}, K_{V\omega, \mathcal{V}_1''}^{(0)}, K_{V\theta, \mathcal{V}_2''}^{(0)}) = (1, 1, 0.01, 5, 1)$. (a): determinant ratio of the controlled system T'' and original system T . (b): change of the first three largest real parts of eigenvalues. Legends $\max \mathcal{R}(\lambda)$, $\max \mathcal{R}_{(2)}(\lambda)$, and $\max \mathcal{R}_{(3)}(\lambda)$ respectively denote the first, second, and third largest real part of eigenvalues. (c) and (d): distribution of rightmost eigenvalues and their movement with the cross-loop control.

VII. CONCLUSIVE REMARKS

This paper investigates the impact of angle-voltage coupling on the stability of inverter-dominant power systems. Our results confirm that the coupling generally contributes to a negative influence on system stability by redistributing the system damping in a more dispersed manner. We built a theoretical tool on the trace and determinant of the state matrix of the linearized system to quantitatively characterize the influence of angle-voltage coupling with interesting insights and appealing implications. Numerically, the angle-voltage coupling conserves total damping d_{Σ} (10) but reduces

the damping redistribution metric κ (16) by 20–80% across systems, redistributing damping dispersively. Besides, κ falls below 1 in 100% of tested systems varying from different scales and operation situations, indicating the wide existence of the coupling's negative influence. The κ threshold of 0.4 serves as a stability indicator: below this, coupling shifts critical eigenvalues rightward by >40% and thus significantly influences the stability evaluation results.

This paper adopts the phasor model in electromechanical transients. However, some recent literature also acknowledges the impact of electromagnetic transient processes on the deterioration of coupled stability. This work focuses on electromechanical transients due to: (i) the mechanism of electromechanical angle-voltage coupling remains nascent and needs detailed investigation, and (ii) the angle-voltage coupling problem is inherently built upon phasor models, and the extension of the latter to the electromagnetic timescale is still an open question [38]. Hence, existing literature usually turns to employ the voltage-current quantities to describe the electromagnetic stability issues. The phasor model is directly defined on the fundamental frequency component, suggesting its descriptive capability is limited around the normal frequencies. Therefore, the proposed method primarily describes the dynamic process of electromechanical transients (± 100 Hz) and struggles to consider higher-frequency oscillations. However, due to the generality of the proposed methodology, it might potentially extend to the cross-timescale coupling dynamics.

Despite its preliminary nature, our work provides a new perspective on understanding, identifying, and controlling angle-voltage coupled power systems. Lastly, distinguished from decoupling controls aimed at recovering a non-coupled system, our theory implies that better dynamics than those of non-coupled systems might be achieved through proper cross-loop controls, which is our future research direction.

REFERENCES

- [1] N. Hatzigyriou, J. Milanovic, C. Rahmann, V. Ajjarapu, C. Canizares, I. Erlich, D. Hill, I. Hiskens, I. Kamwa, B. Pal, P. Pourbeik, J. Sanchez-Gasca, A. Stankovic, T. Van Cutsem, V. Vittal, and C. Vournas, “Definition and Classification of Power System Stability - Revisited & Extended,” *IEEE Transactions on Power Systems*, 2021.
- [2] S. Dong, A. Hoke, B. Wang, L. Ding, X. Lu, C. J. Kruse, B. W. Rockwell, and J. Tan, “A twin circuit theory-based framework for oscillation event analysis in inverter-dominated power systems with case study for kaua’i system,” *IEEE Transactions on Circuits and Systems I: Regular Papers*, pp. 1–14, 2025.
- [3] F. Zhao, X. Wang, and T. Zhu, “Power Dynamic Decoupling Control of Grid-Forming Converter in Stiff Grid,” *IEEE Transactions on Power Electronics*, vol. 37, no. 8, pp. 9073–9088, 2022.
- [4] L. Fan, Z. Wang, and Z. Miao, “Large angle deviation in grid-following ibrs upon grid voltage dip,” *IEEE Transactions on Energy Conversion*, vol. 39, no. 1, pp. 368–378, 2024.
- [5] G. Revel, A. E. Leon, D. M. Alonso, and J. L. Moiola, “Bifurcation analysis on a multimachine power system model,” *IEEE Transactions on Circuits and Systems I: Regular Papers*, vol. 57, no. 4, 2010.
- [6] H. Gao, H. Xin, G. Hu, B. Cao, H. Yuan, and L. Huang, “Common-Mode Frequency of Power Systems Affected by Voltage Dynamics,” *IEEE Transactions on Power Delivery*, pp. 1–13, 2024.
- [7] L. Chen, X. Xie, J. He, T. Xu, D. Xu, and N. Ma, “Wideband oscillation monitoring in power systems with high-penetration of renewable energy sources and power electronics: A review,” *Renewable and Sustainable Energy Reviews*, vol. 175, p. 113148, 2023.
- [8] W. Si, W. Li, N. Tashakor, and J. Fang, “Joint Transient Angle and Voltage Stability Analysis and Enhancement of Grid-Forming Converters,” *IEEE Transactions on Industrial Electronics*, pp. 1–12, 2024.
- [9] M. Li, Y. Wang, W. Hu, S. Shu, P. Yu, Z. Zhang, and F. Blaabjerg, “Unified modeling and analysis of dynamic power coupling for grid-forming converters,” *IEEE Transactions on Power Electronics*, 2021.
- [10] Y. Zhou, T. Xu, L. Ye, M. Liu, X. Chen *et al.*, “Transient Rotor Angle and Voltage Stability Discrimination Based on Deep Convolutional Neural Network with Multiple Inputs,” in *2021 IEEE 4th International Electrical and Energy Conference*, 2021, pp. 1–6.
- [11] Z. Zheng, Q. Bu, C. Shen, and Y. Liu, “Locating Sources of Oscillations Induced by Control of Voltage Source Converters Based on Energy Structure and Nonlinearity Detection,” *Journal of Modern Power Systems and Clean Energy*, pp. 1–10, 2023.
- [12] K. Sharafutdinov, L. Rydin Gorjão, M. Matthiae, T. Faulwasser, and D. Withaut, “Rotor-angle versus voltage instability in the third-order model for synchronous generators,” *Chaos: An Interdisciplinary Journal of Nonlinear Science*, vol. 28, no. 3, p. 033117, 2018.
- [13] M. Thümler, X. Zhang, and M. Timme, “Absence of pure voltage instabilities in the third order model of power grid dynamics,” *Chaos: An Interdisciplinary Journal of Nonlinear Science*, vol. 32, no. 4, p. 043105, 2022.
- [14] P. C. Böttcher, D. Withaut, and L. Rydin Gorjão, “Dynamic stability of electric power grids: Tracking the interplay of the network structure, transmission losses, and voltage dynamics,” *Chaos: An Interdisciplinary Journal of Nonlinear Science*, vol. 32, no. 5, p. 053117, 2022.
- [15] P. Yang, F. Liu, Z. Wang, S. Wu, and H. Mao, “Spectral Analysis of Network Coupling on Power System Synchronization with Varying Phases and Voltages,” in *2020 Chinese Control And Decision Conference (CCDC)*. Hefei, China: IEEE, 2020, pp. 880–885.
- [16] R. A. Horn and C. R. Johnson, *Matrix Analysis*, 2nd ed. New York, NY: Cambridge University Press, 2012.
- [17] H.-D. Chiang, *Direct Methods for Stability Analysis of Electric Power Systems: Theoretical Foundation, BCU Methodologies, and Applications*. John Wiley & Sons, 2010.
- [18] Z. Shuai, C. Shen, X. Liu, Z. Li, and Z. J. Shen, “Transient Angle Stability of Virtual Synchronous Generators Using Lyapunov’s Direct Method,” *IEEE Transactions on Smart Grid*, vol. 10, no. 4, pp. 4648–4661, 2019.
- [19] P. Yang, F. Liu, Z. Wang, and C. Shen, “Distributed Stability Conditions for Power Systems With Heterogeneous Nonlinear Bus Dynamics,” *IEEE Transactions on Power Systems*, vol. 35, no. 3, pp. 2313–2324, 2020.
- [20] Y.-H. Moon, B.-K. Choi, and T.-H. Roh, “Estimating the domain of attraction for power systems via a group of damping-reflected energy functions,” *Automatica*, vol. 36, no. 3, pp. 419–425, 2000.
- [21] W. Ding, C. He, H. Geng, and Y. Liu, “A Novel Lyapunov Function for Transient Synchronization Stability Analysis of Grid-Following Converters,” *IEEE Transactions on Power Systems*, 2025.
- [22] F. Milano, B. Alhanjari, and G. Tzounas, “Enhancing Frequency Control Through Rate of Change of Voltage Feedback,” *IEEE Transactions on Power Systems*, vol. 39, no. 1, pp. 2385–2388, 2024.
- [23] R. Bernal and F. Milano, “Improving Voltage and Frequency Control of DERs through Dynamic Power Compensation,” in *23rd Power Systems Computation Conference*, Paris, France, 2024.
- [24] X. He, V. Häberle, and F. Dörfler, “Complex-Frequency Synchronization of Converter-Based Power Systems,” *IEEE Transactions on Control of Network Systems*, pp. 1–12, 2024.
- [25] M. Farrokhabadi, C. A. Canizares, and K. Bhattacharya, “Frequency Control in Isolated/Islanded Microgrids Through Voltage Regulation,” *IEEE Transactions on Smart Grid*, vol. 8, no. 3, pp. 1185–1194, 2017.
- [26] M. Colombino, D. Groß, J.-S. Brouillon, and F. Dörfler, “Global Phase and Magnitude Synchronization of Coupled Oscillators With Application to the Control of Grid-Forming Power Inverters,” *IEEE Transactions on Automatic Control*, vol. 64, no. 11, pp. 4496–4511, 2019.
- [27] W. Zhong, G. Tzounas, and F. Milano, “Improving the Power System Dynamic Response Through a Combined Voltage-Frequency Control of Distributed Energy Resources,” *IEEE Transactions on Power Systems*, vol. 37, no. 6, pp. 4375–4384, 2022.
- [28] P. S. Kundur, *Power System Stability and Control*, 1st ed. New York: McGraw Hill, 1994.
- [29] X. Peng, F. Liu, P. Yang, P. Yu, K. Luo, and Z. Wang, “Measuring Short-term Voltage Stability of Power Systems Dominated by Inverter-based Resources Part I: System-wise Generalized Voltage Damping Index,” *Journal of Modern Power System and Clean Energy*, 2025.
- [30] J. Schiffer, D. Zonetti, R. Ortega, A. M. Stanković, T. Sezi, and J. Raisch, “A survey on modeling of microgrids—From fundamental physics to phasors and voltage sources,” *Automatica*, vol. 74, pp. 135–150, 2016.

- [31] X. Peng, C. Fu, P. Yang, X. Ru, and F. Liu, "Impact of Angle-Voltage Coupling on Small-Signal Stability of Power Systems: A Damping Perspective," <https://github.com/lingo01/DampingRedistribution>.
- [32] F. Milano, "Complex Frequency," *IEEE Transactions on Power Systems*, vol. 37, no. 2, pp. 1230–1240, 2022.
- [33] L. Zhang, L. Harnefors, and H.-P. Nee, "Power-Synchronization Control of Grid-Connected Voltage-Source Converters," *IEEE Transactions on Power Systems*, vol. 25, no. 2, pp. 809–820, 2010.
- [34] P. Yang, "Augmented Synchronization Based Stability Theory and Its Distributed Analytics of Power Systems," Ph.D. dissertation, Tsinghua University, Beijing, 2022.
- [35] H. Bosetti and S. Khan, "Transient Stability in Oscillating Multi-Machine Systems Using Lyapunov Vectors," *IEEE Transactions on Power Systems*, vol. 33, no. 2, pp. 2078–2086, 2018.
- [36] Y. Song, D. J. Hill, and T. Liu, "Network-Based Analysis of Small-Disturbance Angle Stability of Power Systems," *IEEE Transactions on Control of Network Systems*, vol. 5, no. 3, pp. 901–912, 2018.
- [37] Z. Peng, J. Wang, D. Bi, Y. Dai, and Y. Wen, "The Application of Microgrids Based on Droop Control With Coupling Compensation and Inertia," *IEEE Transactions on Sustainable Energy*, vol. 9, no. 3, pp. 1157–1168, 2018.
- [38] F. Milano, G. Tzounas, and I. Dassios, "Instantaneous Power Theory Revisited with Classical Mechanics," 2024.



Xi Ru received the B.Sc. degree in electrical engineering in 2022 from Tsinghua University, Beijing, China, where she is currently pursuing the Ph.D. degree with the Department of Electrical Engineering. Her research interests include passivity-based stability analysis and control of power systems.



Xiaoyu Peng received the B.Sc. degree in electrical engineering in 2023 from Tsinghua University, Beijing, China, where he is currently pursuing the Ph.D. degree. His research interests include distributed stability analysis and control of phase-angle and voltage dynamics in inverter-dominant power systems.



Cong Fu is a senior engineer with the Control and Dispatch Center of Guangdong Power Grid Corporation. His research interests include the stability analysis and optimized dispatch of power systems integrated with renewable energy resources.



Feng Liu (M'10–SM'18, IEEE) received the B.Sc. and Ph.D. degrees in electrical engineering from Tsinghua University, Beijing, China, in 1999 and 2004, respectively. He is currently an Associate Professor at Tsinghua University. From 2015 to 2016, he was a visiting associate at the California Institute of Technology, CA, USA. Dr. Feng Liu's research interests include stability analysis, optimal control, robust dispatch, and game theory-based decision-making in energy and power systems. He is the author/coauthor of more than 300 peer-reviewed technical papers and four books and holds more than 30 issued/pending patents. Dr. Liu is an IET Fellow. He is an associate editor of several international journals, including *IEEE Transactions on Power Systems*, *IEEE Transactions on Smart Grid*, and *Control Engineering Practice*. He also served as a guest editor of *IEEE Transactions on Energy Conversion*. Dr. Feng Liu was the recipient of the outstanding AE award of *IEEE Transactions on Smart Grid* (Top 3, 2023), the best paper award of *IEEE Transactions on Power Systems* (2018–2020) and several international conferences.



Peng Yang received the B.Sc. degree in electrical engineering, the B.Sc. degree in applied mathematics, and the Ph.D. degree in electrical engineering from Tsinghua University, Beijing, China, in 2017, 2018, and 2022, respectively. He is currently an Associate Professor with the School of Electronics and Information, Xi'an Polytechnic University. His research interests include power system stability analysis and control. Dr. Yang is the winner of the 2020 Zhang SiYing (CCDC) Outstanding Young Paper Award. He is also the recipient of the 2018–2020 Best Paper Award of *IEEE Transactions on Power Systems*.

APPENDIX A COEFFICIENT MATRICES IN STATE MATRIX

The coefficient matrices of the linearized state matrix T are entry-wise defined as follows:

$$A_{ij} = \left(\frac{\partial P}{\partial \theta} \right)_{ij} = \begin{cases} \sum_{k \neq i} B_{ik} V_i^* V_k^* \cos \theta_{ik}^* & \text{if } i = j \\ -B_{ij} V_i^* V_j^* \cos \theta_{ij}^* & \text{if } i \neq j \end{cases} \quad (29)$$

$$C_{1,ij} = \left(\frac{\partial Q/V}{\partial V} \right)_{ij} = \begin{cases} -B_{ii} & \text{if } i = j \\ -B_{ij} \cos \theta_{ij}^* & \text{if } i \neq j \end{cases} \quad (30)$$

$$C_{2,ij} = \left(\frac{\partial Q}{\partial V} \right)_{ij} = \begin{cases} -2B_{ii} V_i^* \\ -\sum_{k \neq i} B_{ik} V_k^* \cos \theta_{ik}^* & \text{if } i = j \\ -B_{ij} V_i^* \cos \theta_{ij}^* & \text{if } i \neq j \end{cases} \quad (31)$$

$$D_{ij} = \left(\frac{\partial P}{\partial V} \right)_{ij} = \left(\frac{\partial Q/V}{\partial \theta} \right)_{ji} = \begin{cases} \sum_{k \neq i} B_{ik} V_k^* \sin \theta_{ik}^*, \text{ if } i = j \\ B_{ij} V_i^* \sin \theta_{ij}^*, \text{ if } i \neq j \end{cases} \quad (32)$$

$$E_{ij} = \left(\frac{\partial Q}{\partial \theta} \right)_{ij} = \begin{cases} \sum_{k \neq i} B_{ik} V_i^* V_k^* \sin \theta_{ik}^* & \text{if } i = j \\ -B_{ij} V_i^* V_j^* \sin \theta_{ij}^* & \text{if } i \neq j \end{cases} \quad (33)$$

APPENDIX B PROOF OF LEMMA 1

Proof. Under the condition $|\theta_{ij}^*| \in (0, \pi/2)$ for $\forall (i, j) \in \mathcal{E}$, A is the Laplacian matrix of a positive-weight undirected graph, thus $A \succ 0$ on D_f . Then, [36] indicates that T_θ is Hurwitz. Besides, the Hurwitzness of the matrix T_V has already been assumed. Then, the non-coupled state matrix $T_n = \text{diag}(T_\theta, T_V)$ is also Hurwitz on \mathcal{D}_f . \square

APPENDIX C PROOF OF THEOREM 1

Lemma 4. Let $A + jdI$ be an $n \times n$ diagonalizable complex matrix, where $A \in \mathbb{R}^{n \times n}$ is symmetrical and $d \in \mathbb{R}$. Then the eigenvectors of $A + jdI$ are real.

Proof. There exists a real orthogonal matrix Q such that $A = Q^T \Lambda Q$, where Λ is a real diagonal matrix. Then we have $A + jdI = Q^T (\Lambda + jd) Q$. In other words, $A + jdI$ could still be diagonalized with real eigenvectors compacted in Q . \square

Lemma 5. The proof is based on [16]. Let A be a diagonalizable matrix and δA a sufficiently small perturbation matrix. Suppose that λ is a simple eigenvalue of A with a corresponding normalized left and right eigenvector w and v . Then, the eigenvalue of $A + \delta A$ is $\lambda + \delta\lambda$, where $\delta\lambda$ is given by $\delta\lambda = w^T \delta A \cdot v$.

Proof. The eigenvector of A satisfies $Av = \lambda v$, $w^T A = \lambda w^T$ and $w^T v = v^T w = 1$. Consider the first-order perturbation of $Av = \lambda v$, written as $\delta A \cdot v + A \cdot \delta v = \delta\lambda \cdot v + \lambda \delta v$. Multiply w^T on both sides and substitute $w^T A = \lambda w^T$ into it, then we have $\delta\lambda = w^T \delta A \cdot v / w^T v = w^T \delta A \cdot v$. \square

Proof of Theorem 1. We first prove the theorem with $g = \mathbb{O}$. Denote a simple eigenvalue of T_n as λ (noting it might be complex), and the corresponding left and right eigenvector as w and v . The eigenvector can be written as the block form

$$\begin{bmatrix} \mathbb{O} & I & \mathbb{O} \\ -M^{-1}A & -M^{-1}d & \mathbb{O} \\ \mathbb{O} & \mathbb{O} & -\tau^{-1}(I + rC_1) \end{bmatrix} \begin{bmatrix} v_1 \\ v_2 \\ v_3 \end{bmatrix} = \lambda \begin{bmatrix} v_1 \\ v_2 \\ v_3 \end{bmatrix} \quad (34)$$

The matrix equation can be equivalently transformed as

$$(\lambda^2 M + \lambda d + A)v_1 = 0, \quad (\lambda\tau + I + rC_1)v_3 = 0 \quad (35)$$

From the left eigenvector w , we can similarly derive the following equations

$$w_2^T M^{-1}(\lambda^2 M + \lambda d + A) = 0, \quad w_3^T \tau^{-1}(\lambda\tau + I + rC_1) = 0 \quad (36)$$

Comparing the above two groups of equations, it is easy to find that v_1 and $w_2^T M^{-1}$ respectively belong to the nullspace and left-nullspace of $\lambda^2 M + \lambda d + A$, and similar for v_3 and $w_3^T \tau^{-1}$ w.r.t. $\lambda\tau + I + rC_1$. Then, we focus on the eigen-space characteristics of both matrices. On the one hand, their imaginary parts might only appear on the diagonal positions induced by $\lambda^2 M$, λd , and $\lambda\tau$. On the other hand, as the identical device parameters r are assumed, the real parts A and rC_1 are symmetrical. Therefore, Lemma 4 indicates the eigenvectors $v_1, M^{-1}w_2$, v_3 and $\tau^{-1}w_3$ are real w.r.t. the eigenvalue $\lambda = 0$.

The angle-voltage coupling perturbs the state matrix from T_n to $T = T_n + T_c$, where T_c plays the role of perturbation matrix in Lemma 5. Therefore, according to the lemma, the eigenvalue perturbation is

$$\begin{aligned} \delta\lambda = w^T T_c v &= [w_1^T, w_2^T, w_3^T] \begin{bmatrix} \mathbb{O} & \mathbb{O} & \mathbb{O} \\ \mathbb{O} & \mathbb{O} & -M^{-1}D \\ -\tau^{-1}rD^T & \mathbb{O} & \mathbb{O} \end{bmatrix} \begin{bmatrix} v_1 \\ v_2 \\ v_3 \end{bmatrix} \\ &= -[(M^{-1}w_2)^T D v_3 + (\tau^{-1}w_3)^T r D^T v_1] \end{aligned} \quad (37)$$

Since the above analysis has indicated that $v_1, v_3, M^{-1}w_2$ and $\tau^{-1}w_3$ are real, now we conclude $\delta\lambda \in \mathbb{R}$ is exactly parallel to the real axis under the condition $g = \mathbb{O}$.

Then we prove the results with the condition $g \neq \mathbb{O}$, the proof of which shares a similar basic idea to Theorem 2. In this situation, the second equation of (35)-(36) are respectively modified as $(\lambda\tau + I + rC_1 + gC_2)v_1 = 0$ and $w_3^T \tau^{-1}(\lambda\tau + I + rC_1 + gC_2) = 0$. If $\mathcal{A}^T V^* = 0$, C_2 is symmetrical and the following proof process is similar. If $\mathcal{A}^T V^*$ is sufficiently small, the continuity of eigenvalues w.r.t. matrix elements guarantees it mainly moves parallel to the real axis, which completes the proof. \square

APPENDIX D PROOF OF THEOREM 2

Lemma 6. Let A, B be $n \times n$ matrices with $A, B \succ 0$. Then we have $|\det(B - A)/\det(A)| = \prod_{i=1}^n |\lambda_i - 1|$, where $\{\lambda_i\}$ is the spectrum of $(\sqrt{A})^{-1} B (\sqrt{A})^{-1}$.⁶

⁶The square root \sqrt{M} of a matrix M is defined by $M = \sqrt{M} \sqrt{M}$. It is always well-defined for a positive-definite symmetrical matrix [16].

Proof. There is a reversible matrix P such that $P^T AP = I$ since $A \succ 0$. Meanwhile, since $P^T BP \succ 0$ still holds, there is a orthogonal matrix Q such that $Q^T P^T BPQ = \text{diag}(\lambda_1, \lambda_2, \dots, \lambda_n) \stackrel{\text{def}}{=} \Lambda$, where $\{\lambda_i\}$ is the spectrum of $P^T BP$. Then we compute its Rayleigh quotient

$$\frac{z^T P^T BP z}{z^T z} \stackrel{x=Pz}{=} \frac{x^T Bx}{x^T (P^{-1})^T P^{-1} x} = \frac{x^T Bx}{x^T Ax} \quad (38)$$

$$\stackrel{\tilde{x}=\sqrt{A}x}{=} \frac{\tilde{x}^T (\sqrt{A})^{-1} B (\sqrt{A})^{-1} \tilde{x}}{\tilde{x}^T \tilde{x}}$$

Now we obtain $\{\lambda_i\}$ is the spectrum of $(\sqrt{A})^{-1} B (\sqrt{A})^{-1}$. Denote $C = PQ$ then we have congruence $C^T AC = I$ and $C^T BC = \Lambda$. Directly compute the determinant, we have $\det(A) = \det(C^{-1} I (C^T)^{-1}) = \det(C)^{-2}$ and

$$\begin{aligned} \det(B - A) &= \det(C^{-1} \Lambda (C^T)^{-1} - C^{-1} I (C^T)^{-1}) \\ &= \det(C^{-1})^2 \cdot \det(\Lambda - I) = \det(C)^{-2} \prod_{i=1}^n |\lambda_i - 1| \end{aligned} \quad (39)$$

Taking their absolute values completes the proof. \square

Proof of Theorem 2. We start with proving the result with the first condition. Recalling the relationship between the determinant and product of eigenvalues, we have

$$\begin{aligned} \prod_i \lambda_i^{(n)} &= \det(T_n) = \det(T_V) \det(T_\theta) \\ \prod_i \lambda_i &= \det(T) = \det(T_V) \det(T_\theta - T_{\theta V} T_V^{-1} T_{V\theta}) \end{aligned} \quad (40)$$

As the T_V -related part is canceled out in the fraction, it is only needed to focus on the T_θ -related part. Direct computation based on (6) yields $\det(T_\theta) = \det(M^{-1}) \cdot \det(-A)$ and

$$\begin{aligned} \det(T_\theta - T_{\theta V} T_V^{-1} T_{V\theta}) &= \det(M^{-1}) \det(-A + D(I + rC_1)^{-1} rD^T) \\ &= \det(M^{-1}) \det(-A + \Xi) \end{aligned} \quad (41)$$

where $\Xi = Dr[r^{-1} - (r + C_1^{-1})^{-1}]rD^T$ and the last step uses the matrix inversion lemma [16]. It is easy to prove $\Xi \succ 0$ with the Sherman-Morrison-Woodbury formula [16]. Then consider the spectrum of Ξ through the quadratic form

$$\begin{aligned} y^T \Xi y &= y^T Dr[I - (I + r^{-1} C_1^{-1})^{-1}] D^T y \\ &= y^T Dr D^T y - y^T Dr(I + r^{-1} C_1^{-1})^{-1} D^T y \\ &\leq \|r\|_\infty \|D\| \|y^T y\| \end{aligned} \quad (42)$$

Therefore, we obtain $0 < \lambda(\Xi) \leq \|r\|_\infty \|D\|$. Then we consider the spectrum of $\tilde{\Xi} = (\sqrt{A})^{-1} \Xi (\sqrt{A})^{-1}$, it satisfies $\lambda_{\min}(\tilde{\Xi}) > 0$ and $\lambda_{\max}(\tilde{\Xi}) = \|(\sqrt{A})^{-1} \Xi (\sqrt{A})^{-1}\| \leq \|(\sqrt{A})^{-1}\| \cdot \|\Xi\| \cdot \|(\sqrt{A})^{-1}\| = \lambda_{\max}(\Xi)/\lambda_{\min}(A)$. Therefore, the spectrum $\{\tilde{\xi}_i\}_i$ of $\tilde{\Xi}$ is bounded by

$$0 < \tilde{\xi}_i < \|r\|_\infty \cdot \|D\| / \lambda_{\min}(A) \leq 1 \quad (43)$$

Then Lemma 6 implies $|\det(T_\theta - T_{\theta V} T_V^{-1} T_{V\theta})/\det(T_\theta)| = \prod_i |\tilde{\xi}_i - 1| \leq 1$, which completes the proof under the first condition.

Then we turn to prove the result under the second condition. For simplification, we start with the easy situation $r = \mathbb{O}$. Furthermore, it is assumed that $V_i^* = V_j^*$ for $\forall (i, j) \in \mathcal{E}$, or equivalently, $\mathcal{A}^T V^* = \mathbb{O}$. The result can be extended

under $V_i^* \neq V_j^*$ using the continuity of the determinant function as $\mathcal{A}^T V^*$ is sufficiently small. A similar analysis yields the following equation $\det(T_\theta - T_{\theta V} T_V^{-1} T_{V\theta}) = \det(M^{-1}) \det(-A + \tilde{\Xi} + D(I - (I + C_2^{-1} g^{-1})^{-1})g\Psi)$, where $\tilde{\Xi} = Dg[g^{-1} - (g + C_2^{-1})^{-1}]gD^T \succ 0$. When $\Psi = \mathbb{O}$, we can derive the desired result with a similar approach under condition $\|g\|_\infty / \lambda_{\min}(A) \leq \|D\|^{-1}$. If $\Psi \neq \mathbb{O}$, the continuity of the determinant function can lead to the same results as long as Ψ is sufficiently small.

Finally, it is noted that the results can be similarly derived when $r \neq \mathbb{O}$, as long as we notice

$$\begin{aligned} &- M^{-1} A + M^{-1} D(rC_1 + gC_2 + I)^{-1} (rD^T + gE) \\ &= -M^{-1} A + M^{-1} D(rC_1 + gC_2 + I)^{-1} rD^T \\ &\quad + M^{-1} D(rC_1 + gC_2 + I)^{-1} gE \\ &= -M^{-1} A + M^{-1} D(rC_1 + gC_2 + I)^{-1} (r + g)D^T \\ &\quad + M^{-1} D(rC_1 + gC_2 + I)^{-1} g\Psi \end{aligned} \quad (44)$$

where $\mathbb{O} \prec (rC_1 + gC_2 + I)^{-1} \prec I$. Similar to the above proof process, $|\det(T_\theta - T_{\theta V} T_V^{-1} T_{V\theta})/\det(T_\theta)|$ is determined by the eigenvalues $\tilde{\xi}'$ of the matrix $\tilde{\Xi}'$, which is defined as $\tilde{\Xi}' = (\sqrt{A})^{-1} D(rC_1 + gC_2 + I)^{-1} (r + g)D^T (\sqrt{A})^{-1}$. Then the eigenvalues can still be bounded by the quadratic form method as follows.

$$0 < \tilde{\xi}'_i \leq \|r + g\| \cdot \|D\| / \lambda_{\min}(A) \leq 1 \quad (45)$$

The other process is similar, which completes the proof. \square

Before ending the section, we discuss the dual formulation of the theorem. In previous proof, the determinant is computed based on (40). Alternatively, it can be reformulated as follows:

$$\begin{aligned} \prod_i \lambda_i^{(n)} &= \det(T_n) = \det(T_\theta) \det(T_V) \\ \prod_i \lambda_i &= \det(T) = \det(T_\theta) \det(T_V - T_{V\theta} T_\theta^{-1} T_{\theta V}) \end{aligned} \quad (46)$$

Then, similar procedures will lead to the following results:

Corollary 2. Given a system \mathcal{G} satisfying the conditions of Lemma 1, then the statements of Theorem 2 still hold if one of the following conditions is satisfied:

- $g = \mathbb{O}$: $\|r\|_\infty / [\lambda_{\min}(A) \lambda_{\min}(C_1)] \leq \|D\|^{-2}$.
- $g \neq \mathbb{O}$: both $\mathcal{A}^T V^*$ and Ψ are sufficiently small, and the following inequality holds

$$\frac{\|r + g\|_\infty}{\lambda_{\min}(A) \cdot \sigma_{\min}(I + rC_1 + gC_2)} \leq \frac{1}{\|D\|^2} \quad (47)$$

where $\sigma_{\min}(\cdot)$ stands for the minimum singular value of a matrix.

Besides, the following term controls the upper bound of the damping redistribution index in a negatively correlated relationship:

$$\|r + g\|_\infty / [\lambda_{\min}(A) \cdot \sigma_{\min}(I + rC_1 + gC_2)] \|D\|^2 \quad (48)$$

The corollary provides a clearer interpretation of the damping redistribution mechanism. As the individual phase-angle and voltage subsystems are strengthened (larger $\lambda_{\min}(A)$ and $\sigma_{\min}(I + rC_1 + gC_2)$) and the coupling reduced (smaller $\|D\|^2$),

the damping redistribution will be weakened. Additionally, the stronger the device-side voltage control is, the less negative influence the coupling will induce. Finally, we point out that the above results can also be extended to the power systems \mathcal{G}' integrated with inverters with first-order phase-angle dynamics by similar analysis procedures in the proof of Theorem 3, which are omitted here for brevity.

APPENDIX E PROOF OF LEMMA 3

Proof. The proof is inspired by [12]. Firstly, the Hurwitzness of T'_V does not change with the form of phase-angle dynamics. Therefore, it is only needed to prove the Hurwitzness of T'_θ . Consider its eigenvalue λ' and corresponding eigenvector satisfying $T'_\theta[\Delta\tilde{\theta}_{\mathcal{V}_1}^T, \Delta\tilde{\omega}_{\mathcal{V}_1}^T, \Delta\tilde{\theta}_{\mathcal{V}_2}^T]^T = \lambda'[\Delta\tilde{\theta}_{\mathcal{V}_1}^T, \Delta\tilde{\omega}_{\mathcal{V}_1}^T, \Delta\tilde{\theta}_{\mathcal{V}_2}^T]^T$. Eliminating the frequency part leads to

$$(A + \Gamma(\lambda')) [\Delta\tilde{\theta}_{\mathcal{V}_1}^T, \Delta\tilde{\theta}_{\mathcal{V}_2}^T]^T = 0 \quad (49)$$

where $\Gamma(\lambda') \stackrel{\text{def}}{=} \text{diag}(\lambda'^2 M + \lambda' d, \zeta + \eta)$, and the extended form of A is given in (21). Similar to Lemma 1, $A \succ 0$ holds on D_f as $|\theta_{ij}^*| \in (0, \pi/2)$ for any $(i, j) \in \mathcal{E}$.

1) If $\lambda' \in \mathbb{R}$: Suppose $\lambda' \geq 0$, then we can derive $A + \Gamma(\lambda') \succ 0$ since $A \succ 0$ and $\Gamma(\lambda') \succeq 0$. Then we conclude $\Delta\tilde{\theta}_{\mathcal{V}_1} = \Delta\tilde{\theta}_{\mathcal{V}_2} = 0$ and further $\Delta\tilde{\omega}_{\mathcal{V}_1} = 0$, which leads to the contradiction.

2) If $\lambda' \in \mathbb{C}/\mathbb{R}$: Denote the first and second equation in (49) as ① and ②. Then we compute $\Delta\tilde{\theta}_{\mathcal{V}_1}^H \times \textcircled{1} - (\Delta\tilde{\theta}_{\mathcal{V}_2}^H \times \textcircled{2})^H$, which yields $\Delta\tilde{\theta}_{\mathcal{V}_1}^H A_{11} \Delta\tilde{\theta}_{\mathcal{V}_1} + \Delta\tilde{\theta}_{\mathcal{V}_1}^H (\lambda'^2 M + \lambda' d) \Delta\tilde{\theta}_{\mathcal{V}_1} = \Delta\tilde{\theta}_{\mathcal{V}_2}^H A_{22} \Delta\tilde{\theta}_{\mathcal{V}_2} + \lambda'^H \Delta\tilde{\theta}_{\mathcal{V}_2}^H \zeta \Delta\tilde{\theta}_{\mathcal{V}_2}$, where superscript H as the Hermite transport. Separating its imaginary part and reducing $\mathcal{I}(\lambda') \neq 0$ from the both sides, we obtain

$$\mathcal{R}(\lambda') = -\frac{\Delta\tilde{\theta}_{\mathcal{V}_1}^H d \Delta\tilde{\theta}_{\mathcal{V}_1} + \Delta\tilde{\theta}_{\mathcal{V}_2}^H \zeta \Delta\tilde{\theta}_{\mathcal{V}_2}}{\Delta\tilde{\theta}_{\mathcal{V}_1}^H M \Delta\tilde{\theta}_{\mathcal{V}_1}} < 0 \quad (50)$$

which completes the proof. \square

APPENDIX F PROOF OF THEOREM 3

Proof. Similar to the proof of Theorem 2, it is only needed to consider $\det(T'_\theta - T'_{\theta V} T_V'^{-1} T_{V\theta}') / \det(T'_\theta)$. We start with computing the determinant of T'_θ

$$\begin{aligned} \det(T'_\theta) &= \det \left(\begin{bmatrix} \mathbb{O} & I & \mathbb{O} \\ -M^{-1} A_{11} & -M^{-1} d & -M^{-1} A_{12} \\ -\zeta^{-1} A_{21} & \mathbb{O} & -\zeta^{-1} (A_{22} + \eta) \end{bmatrix} \right) \\ &= \det \left(\begin{bmatrix} -M^{-1} A_{11} & -M^{-1} A_{12} \\ -\zeta^{-1} A_{21} & -\zeta^{-1} (A_{22} + \eta) \end{bmatrix} \right) \\ &= \det(M^{-1}) \det(\zeta^{-1}) \det(-A') \end{aligned} \quad (51)$$

Then we compute $\det(T'_\theta - T'_{\theta V} T_V'^{-1} T_{V\theta}')$, as shown in (52). The subscript $1, 2$ and $*$ represent $\mathcal{V}_1, \mathcal{V}_2$ and \mathcal{V}' respectively in the above two equations. Then, the form is consistent with Theorem 2 if replacing A' as A . The following proofs are similar, which completes the proof. \square

APPENDIX G PROOF OF THEOREM 4

Proof. This part has used the determinant derivative formula as follows, the proof of which can be found in [16].

$$\frac{d}{d\varepsilon} \det(A(\varepsilon)) = \det(A(\varepsilon)) \cdot \text{Tr} \left(A(\varepsilon)^{-1} \frac{dA}{d\varepsilon} \right). \quad (53)$$

The linearized state matrix T'' of system \mathcal{G}'' is

$$\begin{bmatrix} \mathbb{O} & I & \mathbb{O} \\ -M^{-1} A & -M^{-1} d & -M^{-1} (D + K_{\omega V}) \\ -\tau^{-1} (r D^T + g E + K_{V\theta}) & -\tau^{-1} K_{V\omega} & -\tau^{-1} (r C_1 + g C_2 + I) \end{bmatrix} \quad (54)$$

Then, its determinant can be computed as

$$\begin{aligned} &\det(T'') / \det(-M^{-1}) \det(-\tau^{-1}) \\ &= \det \left(\begin{bmatrix} A & D + K_{\omega V} \\ r D^T + g E + K_{V\theta} & r C_1 + g C_2 + I \end{bmatrix} \right) = \det(J + K_{\text{cl}}) \end{aligned} \quad (55)$$

The determinant ratio is denoted as Φ , and the value w.r.t. the cross-loop control $K_{\text{cl}} = \sigma K_{\text{cl}}^{(0)}$ as $\Phi(\sigma)$. It is clear that $\Phi(0) = 1$ corresponds to the original system \mathcal{G} . Then Φ is computed as

$$\Phi = \left| \frac{\det(T'') / \det(T_n'')}{\det(T) / \det(T_n)} \right| = \left| \frac{\det(T'')}{\det(T)} \right| = \left| \frac{\det(J + K_{\text{cl}})}{\det(J)} \right| \quad (56)$$

We further have

$$\begin{aligned} \frac{d}{d\sigma} \det(J + K_{\text{cl}}) &= \frac{d}{d\sigma} \det(J + \sigma K_{\text{cl}}^{(0)}) \\ &= \det(J + \sigma K_{\text{cl}}^{(0)}) \cdot \text{Tr}[(J + \sigma K_{\text{cl}}^{(0)})^{-1} \frac{d}{d\sigma} (J + \sigma K_{\text{cl}}^{(0)})] \\ &= \det(J + \sigma K_{\text{cl}}^{(0)}) \cdot \text{Tr}[(J + \sigma K_{\text{cl}}^{(0)})^{-1} K_{\text{cl}}^{(0)}] \end{aligned} \quad (57)$$

At $\sigma = 0$, it specifically yields the following (58), where $\text{Tr}(J^{-1} K_{\text{cl}}^{(0)}) \neq 0$ has been assumed in the condition.

$$\frac{d}{d\sigma} \left[\frac{\det(J + \sigma K_{\text{cl}}^{(0)})}{\det(J)} \right]_{\sigma=0} = \text{Tr}(J^{-1} K_{\text{cl}}^{(0)}) \quad (58)$$

Now we turn to study the signs of $\det(J + \sigma K_{\text{cl}}^{(0)})$. Since $\det(J) > 0$ has been assumed, it can be derived that as σ is sufficiently small, the inequality $\det(J + \sigma K_{\text{cl}}^{(0)}) > 0$ also holds with utilizing the continuity of the determinant function. Combining it with $\det(J) > 0$, (58) leads to $\Phi(\sigma) = \det(J + \sigma K_{\text{cl}}^{(0)}) / \det(J)$. Then there exists a sufficiently small σ_0 s.t.

$$\Phi(\sigma_0) - \Phi(0) = \begin{cases} \int_0^{\sigma_0} \frac{d}{d\sigma} \Phi(0) d\sigma, & \text{if } \text{Tr}(J^{-1} K_{\text{cl}}^{(0)}) > 0 \\ \int_{\sigma_0}^0 \frac{d}{d\sigma} \Phi(0) d\sigma, & \text{if } \text{Tr}(J^{-1} K_{\text{cl}}^{(0)}) < 0 \end{cases} \quad (59)$$

Then $\Phi(\sigma_0) > \Phi(0)$ completes the proof. \square

Before ending the section, we further discuss the applicability of the theorem. In practical power systems, $\text{Tr}(J^{-1} K_{\text{cl}}^{(0)}) = 0$ rarely happens and could be avoided by re-selecting a proper $K_{\text{cl}}^{(0)}$ for initialization. As for the other condition, J can be viewed as the quasi-steady power flow Jacobi matrix as shown below:

$$\begin{bmatrix} \Delta P \\ g \Delta Q + r \Delta Q_c \end{bmatrix} = \begin{bmatrix} \frac{\partial P}{\partial \theta} & \frac{\partial P}{\partial V} \\ g \frac{\partial Q}{\partial \theta} + r \frac{\partial Q/V}{\partial \theta} & g \frac{\partial Q}{\partial V} + r \frac{\partial Q/V}{\partial V} + I \end{bmatrix} \begin{bmatrix} \Delta \theta \\ \Delta V \end{bmatrix} \quad (60)$$

$$\begin{aligned}
\det(T'_\theta - T'_{\theta V} T_V'^{-1} T_{V\theta}') &= \det \left(T'_\theta + \begin{bmatrix} \mathbb{O} \\ M^{-1} D_{1*} \\ \zeta^{-1} D_{2*} \end{bmatrix} (rC_1 + gC_2 + I)^{-1} [(rD^T + gE)_{*1} \quad \mathbb{O} \quad (rD^T + gE)_{*2}] \right) \\
&= \det \left(T'_\theta + \begin{bmatrix} \mathbb{O} & \mathbb{O} & \mathbb{O} \\ M^{-1} D_{1*} (rC_1 + gC_2 + I)^{-1} (rD^T + gE)_{*1} & \mathbb{O} & M^{-1} D_{1*} (rC_1 + gC_2 + I)^{-1} (rD^T + gE)_{*1} \\ \zeta^{-1} D_{2*} (rC_1 + gC_2 + I)^{-1} (rD^T + gE)_{*2} & \mathbb{O} & \zeta^{-1} D_{2*} (rC_1 + gC_2 + I)^{-1} (rD^T + gE)_{*2} \end{bmatrix} \right) \quad (52) \\
&= \det(M^{-1}) \det(\zeta^{-1}) \det \left(-A + \text{diag}(\mathbb{O}, \eta) + \begin{bmatrix} D_{1*} \\ D_{2*} \end{bmatrix} (rC_1 + gC_2 + I)^{-1} [(rD^T + gE)_{*1} \quad (rD^T + gE)_{*2}] \right) \\
&= \det(M^{-1}) \det(\zeta^{-1}) \det(-A' + D(rC_1 + gC_2 + I)^{-1}(rD^T + gE))
\end{aligned}$$

where the power change attributed to the device voltage control is $\Delta Q_c = \Delta(Q/V) + r^{-1}\Delta V$. Therefore, it is reasonable to assume all eigenvalues of J have positive real parts as the system has a stable equilibrium, which leads to $\det(J) > 0$.

APPENDIX H SIMULATION SETTINGS, DATA GENERATION, AND SOURCE CODE

All simulations and data processing are performed on MATLAB. The authors promise that all data and codes to generate the results in this paper have been open-sourced on https://github.com/lingo01/Damping_Redistribution.

A. Simulation Models and Settings

The topology and network configurations, including the admittance matrix, are directly derived from the default database of MATPOWER.

The flux-decay SG and virtual-SG are modeled by (61), where x_{di} , x'_{di} , T'_{di} , and b_i represent the d-axis synchronous reactance, transient reactance, q-axis open-circuit transient time constant, and shunt capacitance, respectively [28]. It can be transformed into the standard form (2) by setting $\tau_i = T'_{di}$, $r_i = x_{di} - x'_{di}$ and $u_i = E_{fi}$. The analysis can be conducted on E'_{qi} instead of V_i if reducing x'_{di} into the network, which is a classical method for stability analysis [19], [28].

$$\begin{aligned}
M_i \ddot{\theta}_i &= -D_i \dot{\theta}_i - P_i + P_i^g \\
T'_{di} \dot{E}'_{qi} &= -E'_{qi} - (x_{di} - x'_{di}) \frac{Q_i}{E'_{qi}} + E_{fi} \quad (61)
\end{aligned}$$

The models of CD inverters are given by the following (62). The dynamics are directly derived from [19], [29]. The same notations are used as in the above literature, and thus, we omit the introduction to save space. Finally, the model can be transformed into the standard one (4) and the voltage dynamics of (2) by setting the parameters $\zeta_i = \tau_{dpP,i}/D_{dpP,i}$, $\eta_i = 1/D_{dpP,i}$, $\tau_i = \tau_{dpQ,i}$, $r_i = 0$ and $g_i = D_{dpQ,i}$.

$$\begin{aligned}
\tau_{dpP,i} \dot{\theta}_i &= -(\theta_i - \theta_{s,i}) - D_{dpP,i} (P_i - P_{s,i}) \\
\tau_{dpQ,i} \dot{V}_i &= -(V_i - V_{s,i}) - D_{dpQ,i} (Q_i - Q_{s,i}) \quad (62)
\end{aligned}$$

The static loads and connecting buses are approximately modeled by the devices with $P - \theta/Q - V$ conventional-droop (CD) control with $(\tau_{dpP,i}, D_{dpP,i}, \tau_{dpQ,i}, D_{dpQ,i}) =$

$(0.05, 100, 0.05, 100)$. This approximation enables the analysis while preserving the network structure. Despite the heterogeneity of devices, their parameters are also nonuniform, thus providing a more practical verification compared to the above theoretical analysis.

B. Outline of Data Generation Procedure

This part outlines the data generation procedure in the simulation section. More details can be found in the open-sourced code.

Eigenvalue Computation: We first introduce the eigenvalue computation of the coupled systems T (λ_i) and the non-coupled systems T_n ($\lambda_i^{(n)}$). After we derive the system simulation model as introduced above, all devices are transformed into the standard form (2). Then, the state matrix T and its non-coupled form T_n can be computed by (6) and (7). Then, their eigenvalues can be computed by directly calling the `eig()` function in MATLAB.

Total/Average Damping Computation: With the state matrix T and its non-coupled form T_n derived, the computation of total damping and average damping is simply done by calling the `trace()` function in MATLAB.

Damping Redistribution Index Computation: We still assume the matrices T and T_n have been obtained. A direct way to compute $|\det(T)/\det(T_n)|$ is to call the `det()` function in MATLAB. However, sometimes $\det(T)$ might be too large to be precisely computed and saved in MATLAB. Therefore, we adopt an alternative way to compute all eigenvalues of T and T_n . Then, the determinant ratio can be recovered by

$$\left| \frac{\det(T)}{\det(T_n)} \right| = \left| \prod_i \frac{\lambda_i}{\lambda_i^{(n)}} \right| \quad (63)$$

APPENDIX I SENSITIVITY ANALYSIS OF REDISTRIBUTION INDEX

As a preparation, we first consider a homotopic map between T_n and T , written as

$$\mathcal{T}(\varepsilon) = (1 - \varepsilon)T_n + \varepsilon T = T_n + \varepsilon T_c \quad (64)$$

Clearly, it satisfies $\mathcal{T}(0) = T_n$ and $\mathcal{T}(1) = T$. In other words, the state matrix changes from the non-coupled to the coupled one as the homotopic factor ε increases from 0 to 1. Denote its real eigenvalues as $-\tilde{\mu}_i$ ($i = 1, 2, \dots, p$) and complex eigenvalues as $-\tilde{\alpha}_i \pm j\tilde{\beta}_i$ ($i = 1, 2, \dots, q$), which satisfy $\tilde{\mu}_i >$

0 and $\tilde{\alpha}_i, \tilde{\beta}_i > 0$. We further sort $\tilde{\mu}_i$ as $\tilde{\mu}_1 < \tilde{\mu}_2 < \dots < \tilde{\mu}_p$. Then the absolute value of the determinant can be expressed as $|\det(\mathcal{T})| = \prod_{i=1}^p \tilde{\mu}_i \prod_i^q (\tilde{\alpha}_i^2 + \tilde{\beta}_i^2)$. Then consider its sensitivity with the factor ε at $\varepsilon = \varepsilon_0$:

$$\begin{aligned} \frac{\partial |\det(\mathcal{T})|}{\partial \varepsilon}(\varepsilon_0) &= \sum_{i=1}^p \frac{\partial |\det(\mathcal{T})|}{\partial \tilde{\mu}_i} \frac{\partial \tilde{\mu}_i}{\partial \varepsilon} + 2 \sum_{i=1}^q \frac{\partial |\det(\mathcal{T})|}{\partial \tilde{\alpha}_i} \frac{\partial \tilde{\alpha}_i}{\partial \varepsilon} \\ &= \det(\mathcal{T}(\varepsilon_0)) \left(\sum_{i=1}^p \frac{1}{\tilde{\mu}_i} \frac{\partial \tilde{\mu}_i}{\partial \varepsilon} + \sum_{i=1}^q \frac{4\tilde{\alpha}_i}{\tilde{\alpha}_i^2 + \tilde{\beta}_i^2} \frac{\partial \tilde{\alpha}_i}{\partial \varepsilon} \right) \end{aligned} \quad (65)$$

Since $\partial |\det(\mathcal{T})| / \partial \mu \propto 1/\mu$, thus these $\mu \approx \infty$ eigenvalues related to $g \approx \infty$ generally do not influence the ratio.

We still assume the eigenvalue moves parallel to the real axis as suggested by Theorem 1, then the change of determinant can be computed by

$$\begin{aligned} |\det(T)| - |\det(T_n)| &= \int_0^1 \frac{\partial |\det(\mathcal{T})|}{\partial \varepsilon} d\varepsilon \\ &= \sum_{i=1}^p \int_0^1 |\det(\mathcal{T})| \frac{1}{\tilde{\mu}_i} \frac{\partial \tilde{\mu}_i}{\partial \varepsilon} d\varepsilon + \sum_{i=1}^q \int_0^1 |\det(\mathcal{T})| \frac{4\tilde{\alpha}_i}{\tilde{\alpha}_i^2 + \tilde{\beta}_i^2} \frac{\partial \tilde{\alpha}_i}{\partial \varepsilon} d\varepsilon \\ &= \sum_{i=1}^p \int_{\mu_i^{(n)}}^{\mu_i} |\det(\mathcal{T})| \frac{1}{\tilde{\mu}_i} d\tilde{\mu}_i + \sum_{i=1}^q \int_{\alpha_i^{(n)}}^{\alpha_i} |\det(\mathcal{T})| \frac{4\tilde{\alpha}_i}{\tilde{\alpha}_i^2 + \tilde{\beta}_i^2} d\tilde{\alpha}_i \end{aligned} \quad (66)$$

where $-\mu_i^{(n)}$ and $-\mu_i$ are respectively the eigenvalue of T_n and T , and analogue to $\alpha_i^{(n)}$ and α_i . In practical power systems, $\tilde{\beta}_i \gg \tilde{\alpha}_i$ usually holds, thus in the above equation we can further use the approximation $4\tilde{\alpha}_i/(\tilde{\alpha}_i^2 + \tilde{\beta}_i^2) \approx 4\tilde{\alpha}_i/\tilde{\beta}_i^2$. Assuming $|\det(\mathcal{T}(\varepsilon))| \approx |\det(T_n)|$ as its relative change is usually small compared to that of eigenvalues, we obtain

$$\frac{|\det(T)| - |\det(T_n)|}{|\det(T_n)|} \approx \sum_{i=1}^p \ln \frac{\mu_i}{\mu_i^{(n)}} + \sum_{i=1}^q \frac{2(\alpha_i^2 - \alpha_i^{(n)2})}{\beta_i^2} \quad (67)$$

where the last term can be omitted as $\tilde{\beta}_i \gg \tilde{\alpha}_i$. Then it yields

$$\begin{aligned} \left| \frac{\det(T)}{\det(T_n)} \right| &\approx 1 + \ln \left(1 + \frac{\mu_1 - \mu_1^{(n)}}{\mu_1^{(n)}} \right) + \sum_{i=2}^p \ln \frac{\mu_i}{\mu_i^{(n)}} \\ &\approx 1 + \frac{\mu_1 - \mu_1^{(n)}}{\mu_1^{(n)}} + \sum_{i=2}^p \ln \frac{\mu_i}{\mu_i^{(n)}} \end{aligned} \quad (68)$$

The last equality uses the approximation $\ln(1 + x) \approx x$ as x is sufficiently small. Since we focus on the most critical damping, we have the following approximated linearity as

$$\left| \frac{\det(T)}{\det(T_n)} \right| \approx \frac{1}{\max \mathcal{R}(\lambda^{(n)})} [\max \mathcal{R}(\lambda) - \max \mathcal{R}(\lambda^{(n)})] + f \quad (69)$$

where $f(\mu_2, \mu_3, \dots, \mu_p)$ is a function independent from μ_1 .